

ADE 900 797

DTIC FILE COPY



NWC TP 6770

Structural Response of Flat Panels to Hydraulic Ram Pressure Loading

by
E. A. Lundstrom
Research Department

FEBRUARY 1968

NAVAL WEAPONS CENTER
CHINA LAKE, CA 93555-0001



Approved for public release; distribution is unlimited.

DTIC
ELECTE
OCT 31 1988
S D

AD-A200 410

88 10 31 68

UNCLASSIFIED

SECURITY CLASSIFICATION OF THIS PAGE (When Data Entered)

AD-A100 410

REPORT DOCUMENTATION PAGE

1a. REPORT SECURITY CLASSIFICATION UNCLASSIFIED			1b. RESTRICTIVE MARKINGS		
2a. SECURITY CLASSIFICATION AUTHORITY			3. DISTRIBUTION/AVAILABILITY OF REPORT Approved for public release; distribution is unlimited.		
2b. DECLASSIFICATION/DOWNGRADING SCHEDULE					
4. PERFORMING ORGANIZATION REPORT NUMBER(S) NWCTP 6770			5. MONITORING ORGANIZATION REPORT NUMBER(S)		
6a. NAME OF PERFORMING ORGANIZATION Naval Weapons Center		6b. OFFICE SYMBOL (If Applicable)	7a. NAME OF MONITORING ORGANIZATION		
6c. ADDRESS (City, State, and ZIP Code) China Lake, CA 93555-6001			7b. ADDRESS (City, State, and ZIP Code)		
8a. NAME OF FUNDING/SPONSORING ORGANIZATION Office of Naval Research		8b. OFFICE SYMBOL (If Applicable)	9. PROCUREMENT INSTRUMENT IDENTIFICATION NUMBER		
8c. ADDRESS (City, State, and ZIP Code) Arlington, VA 22217			10. SOURCE OF FUNDING NUMBERS		
			PROGRAM ELEMENT NO.	PROJECT NO	TASK NO RR00001
			WORK UNIT NO		
11. TITLE (Include Security Classification) STRUCTURAL RESPONSE OF FLAT PANELS TO HYDRAULIC RAM PRESSURE LOADING (U)					
12. PERSONAL AUTHOR(S) Lundstrom, E. A.					
13a. TYPE OF REPORT Final		13b. TIME COVERED From Oct 84 To Oct 86		14. DATE OF REPORT (Year, Month, Day) 1988, February	
15. PAGE COUNT 62					
16. SUPPLEMENTARY NOTATION					
17. COSATI CODES			18. SUBJECT TERMS (Continue on reverse side if necessary and identify by block number)		
FIELD	GROUP	SUB-GROUP			
			Aircraft Structure Structural Response		
			Hydraulic Ram Pressure Loading		
19. ABSTRACT (Continue on reverse side if necessary and identify by block number)					
<p>(U) The theory for hydraulic ram effects in fuel tanks impacted by high-speed projectiles is extended. Experiments were performed with a simple, highly instrumented water tank and the test results compared with theoretical predictions. The comparison was good for hydraulic ram pressure in the water tank and for strain in the water tank walls. Predictions of catastrophic failure in the aluminum wall panels were in agreement with observations.</p> <p>(U) The extended theory allows calculation for multiple impacts of projectiles that are supersonic with respect to the fluid. Energy-absorbing foam and air gaps at the fluid/structure interface are now included in the theory. Effects of dynamic cavitation at the fluid/structure interface on pressure loading are accounted for. (AW)</p>					
20. DISTRIBUTION/AVAILABILITY OF ABSTRACT <input checked="" type="checkbox"/> UNCLASSIFIED/UNLIMITED <input type="checkbox"/> SAME AS RPT. <input type="checkbox"/> DTIC USERS			21. ABSTRACT SECURITY CLASSIFICATION Unclassified		
22a. NAME OF RESPONSIBLE INDIVIDUAL Eric Lundstrom			22b. TELEPHONE (Include Area Code) 619-939-2206		22c. OFFICE SYMBOL Code 3894

Figures:

BTIC
COPY
INSPECTED
6

list

A-1

NWC TP 6770

12. Pressure Gage Record No. 2 for Shot 239	36
13. Pressure Gage Record No. 3 for Shot 239	36
14. Pressure Gage Record No. 4 for Shot 239	37
15. Pressure Gage Record No. 5 for Shot 239	37
16. Pressure Plot at 0.1 Millisecond After Impact, Shot 239	38
17. Pressure Plot at 0.5 Millisecond After Impact, Shot 239	39
18. Pressure Plot at 1.3 Milliseconds After Impact, Shot 239	39
19. Fluid Velocity at 0.1 Millisecond After Impact, Shot 239	40
20. Fluid Velocity at 1.0 Millisecond After Impact, Shot 239	40
21. Gaussian Panel Deflection Showing Resulting Peak Deflection	41
22. Motion of Center of Gaussian Panel Deflection	42
23. Widths of Gaussian Profile in x and y Directions	42
24. Weighted Averages of Incident Pressure and Normal Fluid Velocity	43
25. Weighted Average of Total Wall Pressure Loading	44
26. Growth and Collapse of Cavitation at Wall	45
27. Average Value of Variable Image Theory Q Function	45
28. Peak Wall Membrane Stresses Calculated at Gaussian Center	46
29. Wall Strain Energy	47
30. Entrance Panel Geometry Showing Location of Strain Gages for Shot 239	47
31. Experimental Strain Gage Data Compared to Corresponding Calculated Strains, No. 239-1	48
32. Experimental Strain Gage Data Compared to Corresponding Calculated Strains, No. 239-2	48
33. Experimental Strain Gage Data Compared to Corresponding Calculated Strains, No. 239-3	49
34. Experimental Strain Gage Data Compared to Corresponding Calculated Strains, No. 239-4	49
35. Experimental Strain Gage Data Compared to Corresponding Calculated Strains, No. 239-5	50
36. Experimental Strain Gage Data Compared to Corresponding Calculated Strains, No. 239-6	50
37. Spatial Distribution of the Incident Pressure	51
38. Spatial Distribution of the Incident Normal Velocity	52
39. Spatial Distribution of the Total Wall Pressure	53
40. Spatial Distribution of the Panel Deflection	54
41. Spatial Distribution of the Wall Cavitation	55
42. Spatial Distribution of the Variable Image Q Function	56
43. Results of Peak Stress Calculation Performed for Both Gaussian and Fixed- Boundary Cosine Panel Deflection Profile Entrance Shot, 0-Degree Obliquity	58
44. Results of Peak Stress Calculation Performed for Both Gaussian and Fixed- Boundary Cosine Panel Deflection Profile Entrance Shot, 45-Degree Obliquity	58
45. Results of Peak Stress Calculation Performed for Both Gaussian and Fixed-Boundary Cosine Panel Deflection Profile Exit Panel, 0-Degree Obliquity ...	59
46. Results of Peak Stress Calculation Performed for Both Gaussian and Fixed-Boundary Cosine Panel Deflection Profile Exit Panel, 45-Degree Obliquity ..	59

Tables:

1. Shot Matrix and Results Summary	34
2. Strain Gage Location and Orientation for Shot 239	47

INTRODUCTION

↖ Aircraft structural surfaces often serve as the walls of integral fuel cells. Projectiles penetrating the fuel generate intense pressure waves capable of producing catastrophic failure of the fuel cell walls. This phenomenon, termed hydraulic ram, can lead to structural kill of the aircraft. Massive fuel loss, resulting from fuel cell failure, can also lead to aircraft kill by on-board fires or by fuel starvation.

↗ Drag forces acting to decelerate the projectile are the source of pressure waves that propagate into the fuel. A prominent characteristic of the fluid flow is a cavity that extends from the projectile back to the impact point. The cavity grows radially away from the trajectory. The cavity eventually collapses, but on a longer time scale than of interest here. The fluid pressure field is highly peaked at the projectile. The fluid velocity field is high at the projectile and near the cavity.

Pressure waves incident upon a fuel cell wall produce reflected waves that depend upon the motion of the wall. The walls, in turn, move in response to the total pressure loading. The coupling between the fluid pressure field and wall motion, called the fluid/structure interaction, is of critical importance with dense, condensed fluids like fuel or water. In contrast, for highly compressible fluids like gases, the fluid/structure interaction can be neglected. In hydraulic ram, the interaction is complicated by cavitation, which occurs in response to negative pressures that can be obtained at the fluid/structure interface.

Motion of a structure can be readily calculated given the pressure loading. However, the structural response to hydraulic ram can include nonlinear deflections and plastic deformations. Fuel cell structure can be either metallic or fiber composite. The construction may include elastomer fuel cell liners. Foam or air gap isolation may be employed between the fuel and the structure. Of interest is the damage that occurs during hydraulic ram: walls may fail catastrophically, joints and rivets may fail, and fiber composites may delaminate in response to bending.

The pressure wave generation theory had its roots in the work of Bristow and Lundeberg (Reference 1) and Yurkovich (Reference 2). Yurkovich, in particular, used the idea of describing the fluid motion by a moving point source in a potential flow. This idea formed the basis of the hydraulic ram pressure theory for subsonic tumbling projectiles. The theory was developed by Lundstrom (Reference 3), who used a moving line of sources whose

strength was based on the projectile drag characteristics. The theory was substantiated by a large body of experimental data obtained by Lundstrom and Fung (References 4 and 5).

Predicting structural response to hydraulic ram pressure loading has proven to be a difficult task. Early work was based on use of the piston theory for the fluid/structure interaction. This theory assumed that pressure waves reflected from fuel tank walls were one-dimensional, and propagated normally away from the wall surface.

Ball (Reference 6) modified two structural analysis computer codes, including the piston theory and hydraulic ram pressure loading. The SATANS code was limited to elastic motion of shells of revolution, but was computationally efficient.

The BR-1 code (Reference 7) was a more general finite element structural code that allowed plastic deformation of the elements. However, this code was very computationally intensive, taking 50 times more computer time than the SATANS program. The BR-1 code version, which included the piston theory, was called the BR-1HR code. Predictions of the BR-1HR and modified SATANS codes were compared with experiments in Reference 8. It was found that experimental strain data greatly exceeded the predicted values. The disagreement was attributed to the failure of the piston theory for hydraulic ram pressure loading.

The Moiré fringe technique was used by Fry, Newman, and Bless (Reference 9) to measure the deflection of entrance panels induced by hydraulic ram. The data were analyzed by Bless, Fry, and Barber (Reference 10) using the BR-1HR program, with results similar to those of Ball.

Since the piston theory failed to describe the fluid/structural interaction in hydraulic ram, Lundstrom (Reference 11) proposed the variable image method. The fluid potential of pressure waves reflected by a moving wall is assumed to be in the form of an image of the incident wave potential multiplied by an unknown function. The function is determined by matching the fluid velocity with the wall velocity at the interface.

At the same time, Ankeney (Reference 12) suggested an approximate structural model for use in hydraulic ram analysis. A panel deflection profile in the shape of a cosine curve was assumed, and then the amplitude was calculated using the Lagrange equations of motion.

Lundstrom modified the pressure wave generation model computer program (Reference 13) to calculate panel deflections. The variable image method (Reference 11) for the fluid/structural reaction was employed, and Ankeney's structural equations (Reference 12) were used for structural response. Computer code predictions of panel deflections were compared with a single exit panel shot in Reference 11. Agreement between code prediction and experiment was quite good. The computer code was called the Unimodal Hydraulic Ram Structural Response (UHRSR) program. A user's manual was published by Ankeney (Reference 14).

The UHRSR code was modified by Wada, Høitz, and Jacobson (Reference 15) to include a capability to calculate the response of orthotropic panels to hydraulic ram pressure loading. Computer calculations of wall deflection and strain were compared with entry panel experimental data. A general lack of agreement was obtained. The predictions of panel

strain were particularly bad. The most probable cause was the fact that panel deflections did not look like the assumed cosine curve.

Herlin and Avery (Reference 16) merged the UHRSR and BR-1FC codes to produce the Hydraulic Ram Structural Response (HRSR) code. The BR-1FC code was an extension of the BR-1 code to include analysis of orthotropic structural elements. Comparisons of the HRSR code calculations with experiments were performed by Bradley and Avery (Reference 17) and Jacobson, Heitz, and Yamane (Reference 18). Reasonable agreement was usually obtained. Discrepancies were primarily attributed to the following:

1. The finite element grid is usually chosen too coarse because the code is very expensive to run. Large pressure gradients near projectile exit or entrance points are not adequately represented.
2. Cavitation at the fluid/structure interface is not accurately modeled.

Fuel tank failure is assumed in the HRSR code whenever the material strain exceeds the ultimate strain. Bradley and Avery (Reference 17) have shown that damage propagation from ballistic perforations can be obtained at much lower strains because of fracture mechanisms. Ball and Fahrenkrog (Reference 19) attempted to use fracture mechanics to calculate the lengths of the cracks in damaged panels. They were handicapped since their use of the piston theory of the fuel/structural interaction gave predicted stresses that were too low. However, they were encouraged by results obtained by normalization of the stresses.

Rosenberg and Bless (Reference 20) have derived an empirical scaling model of hydraulic ram failure based solely on fracture mechanics considerations.

This work was intended to extend the HRSR code to include multiple supersonic projectiles. The HRSR code, however, proved to be very difficult to run and inconvenient to use. The UHRSR code was available, and modifications had already been incorporated. Extensions were made to the fluid/structural interaction model to include cavitation, and the structural model was generalized to widen its application. The resulting computer program is called the ERAM code. This code will be documented at another time.

The new developments in the hydraulic ram theory are presented in this report. Experiments were performed using nontumbling cylindrical projectiles to give repeatable data for exit and entrance panel shots at 0- and 45-degree obliquity. One of the shots, an entrance shot at 45 degrees, is analyzed extensively. Predictions of fluid pressure and aluminum panel strains are compared to experimental data. Plots of the hydraulic ram variables within the fluid and at the fluid/structure interface are made to illustrate the dynamic interaction of the fluid mechanics and the fuel cell structure.

Fracture mechanics techniques are applied to predict panel catastrophic failure thresholds with some success.

PRESSURE WAVE GENERATION

The theory for the pressure wave generation for single subsonic penetrators during the drag phase of hydraulic ram was presented earlier in References 3 and 4. The user's manual for a computer code implementing the theory (Reference 13) contains the derivation additional equations required for the numerical evaluation of hydraulic ram pressures. The theory has been extended to multiple supersonic projectiles. The intent of this section is to document the extension to supersonic projectiles in some detail, but without reproducing all of the mathematics for subsonic projectiles.

The hydraulic ram theory assumes that the flow field can be described in terms of a potential function, ϕ , which satisfies the wave equation

$$\nabla^2 \phi = \frac{1}{c^2} \frac{\partial^2 \phi}{\partial t^2} \quad (1)$$

where c is the sound speed in the fluid. In terms of the potential, the fluid velocity, \vec{u} , is given by

$$\vec{u} = \nabla \phi \quad (2)$$

and the pressure, p , is obtained from Bernoulli's equation

$$p = p_0 - \rho \frac{\partial \phi}{\partial t} - \frac{1}{2} \rho u^2 \quad (3)$$

where p_0 is the ambient pressure and ρ is the fluid density.

The coordinate system for the analysis is shown in Figure 1. The coordinate of an arbitrary point is (x, ω) , where ω is the perpendicular distance to the trajectory and x is the distance parallel to the trajectory. The origin of the coordinate system is the impact point.

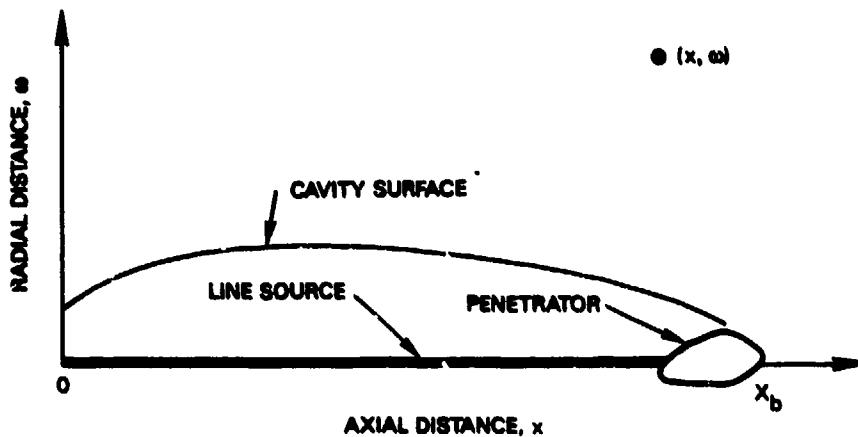


FIGURE 1. Geometry for Pressure Wave Generation Model.

The simplifying approach of the model is to try to approximate the effect of the projectile and cavity by a line of sources distributed along the trajectory path behind the projectile. The potential for an arbitrary line-source distribution is given by the integral

$$\phi(x, \omega, t) = - \int_{X_a(t)}^{X_b(t)} \frac{\zeta(\xi, \tau)}{r} d\xi \quad (4)$$

where ξ is the distance along the trajectory, r is the distance from $(\xi, 0)$ to (x, ω) , and ζ is the source strength at ξ . Since ξ satisfies the wave equation, the source strength and integration limits must be evaluated at the retarded time $\tau = t - r/c$.

The integral in Equation 4 is a line integral over a path defined by $\tau = t - r/c$ with the time, t , held constant. Figure 2 shows the geometry of a typical integration path on the time-space plane. For a given drag force history, the projectile time of arrival can be calculated as a function of projectile position, X_b . A representative trajectory for a subsonic penetrator is included in Figure 2. For the subsonic case, the integration path intersects the trajectory at a maximum of one point. This point is the upper integration limit X_b , which is the projectile position at time $\tau = t_b$. The line-source distribution extends to the impact point, so the lower integration limit is $X_a = 0$.

The geometry is more complicated for the case of supersonic penetrators. The trajectory and integration path will have multiple intersections for certain choices of (x, ω, t) .

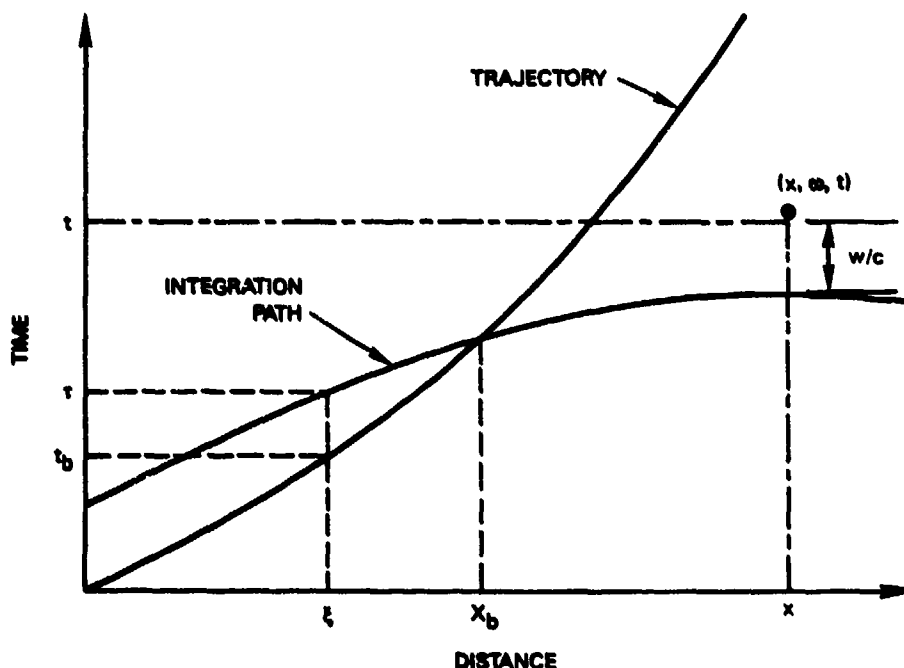


FIGURE 2. Geometry for Typical Integration Path on Time-Space Plane. Also shown is the trajectory for a subsonic penetrator.

This situation is illustrated in Figure 3. Three integration paths are shown corresponding to three successive times. For the integration path labeled t_0 , the trajectory is tangent to the integration path. At time t_0 , pressure disturbances produced by the projectile first reach the point (x, ω) . The integration limits $X_b = X_a$. Because of the tangency, the integral will be singular, as will be seen below. At a later time, $t_1 > t_0$, the intersection points have separated. One integrates between limits $X_b(t_1) > X_a(t_1)$.

For subsonic penetrators, the integral (Equation 4) for the fluid potential is taken between limits $X_b(t)$ and 0. For supersonic penetrators, the integral can be partitioned into two similar integrals

$$\begin{aligned} \phi(x, \omega, t) = & - \int_0^{X_b(t)} \frac{\zeta(\xi, t)}{r} d\xi \\ & + \int_0^{X_a(t)} \frac{\zeta(\xi, t)}{r} d\xi \end{aligned} \quad (5)$$

Both integrals are identical to the subsonic case, so that, in principle, the subsonic results are directly applicable. However, required derivatives of ϕ are singular at the sonic point. The singularities arise from the Doppler shift of waves produced by the penetrator. The

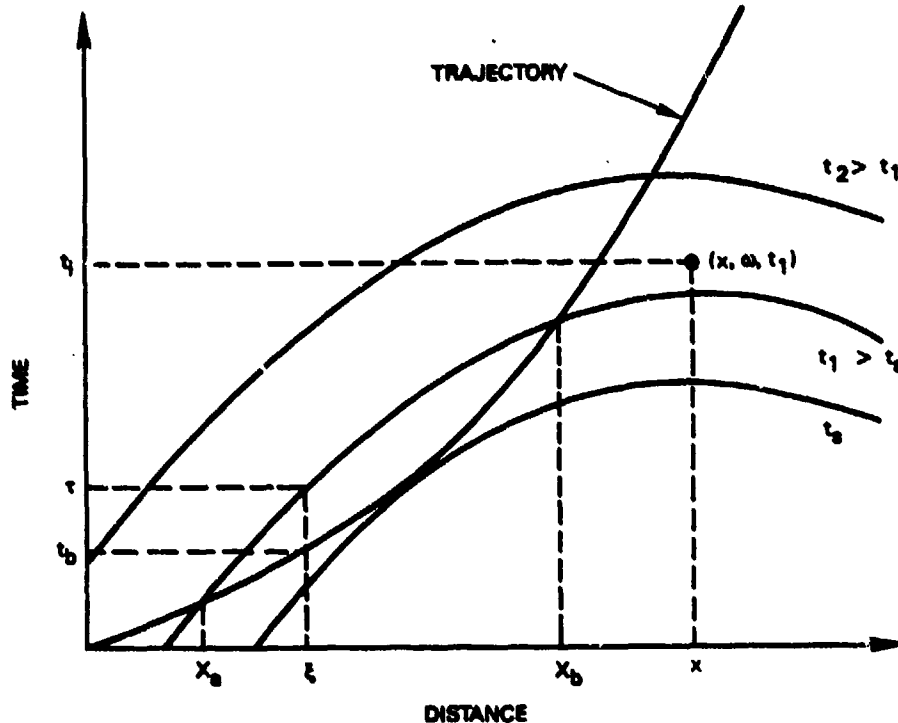


FIGURE 3. Sequence of Integration Curves for the Potential at (x, ω) for Times $t_0 < t_1 < t_2$. The trajectory for the supersonic penetrator may intersect the integration curve twice, as shown for the curve t_1 .

singularities are resolved in nature by nonlinear terms neglected in the approximate wave equation for ϕ .

The source distribution was derived in References 3 and 13 as

$$\zeta(\xi, t) = \frac{1}{2}BA(\xi) - \frac{1}{2}B^2[t - t_b(\xi)] \quad (6)$$

where $A(\xi)$ is the maximum cavity radius obtained along the trajectory, and $t_b(\xi)$ is the projectile time of arrival at point ξ . The function $A(\xi)$ is given by

$$A^2(\xi) = \frac{\left(\frac{dE}{dX_b}\right)_\xi}{n(P_o - P_c)} \quad (7)$$

where the derivative $(dE/dX_b)_\xi$ is the rate at which the projectile kinetic energy is deposited into the fluid by the drag forces. The ambient and cavity pressures are denoted by P_o and P_c , respectively. The constant B has dimensions of velocity and is given by

$$B^2 = \frac{P_o - P_c}{\rho N} \quad (8)$$

where N is a geometric dimensionless parameter discussed in Reference 3. A value of $N = 1/0.434$ is used in the computer program.

To obtain the fluid potential, Equation 6 is substituted into Equation 4 (or Equation 5 for supersonic penetrators), which could then be integrated. However, for the desired fluid pressure and velocity, derivatives of the potential ϕ are required. In References 3 and 13, expressions for these derivatives were derived as

$$\frac{\partial \phi}{\partial x} = -\frac{BA_b}{2R_b} \frac{\frac{V_b}{1 - \frac{V_b}{c} \frac{x - X_b}{R_b}}}{\frac{V_b}{1 - \frac{V_b}{c} \frac{x - X_b}{R_b}}} + \frac{B^2}{2} \ln\left(\frac{x + R_o}{x - X_b + R_b}\right) \quad (9)$$

$$\frac{\partial \phi}{\partial \omega} = \frac{BA_b}{2R_b} \frac{\frac{\frac{V_b}{c} \frac{\omega}{R_b}}{1 - \frac{V_b}{c} \frac{x - X_b}{R_b}}}{\frac{V_b}{1 - \frac{V_b}{c} \frac{x - X_b}{R_b}}} + \frac{B}{2} I_\omega \quad (10)$$

$$\frac{\partial \phi}{\partial x} = \frac{BA_b}{2R_b} \frac{\frac{\frac{V}{c} \frac{x - X_b}{R_b}}{1 - \frac{V_b}{c} \frac{x - X_b}{R_b}}}{\frac{V_b}{1 - \frac{V_b}{c} \frac{x - X_b}{R_b}}} + \frac{B}{2} I_x \quad (11)$$

where

$$I_{\omega} = \int_0^{X_b} [A - B(t - t_b)] \frac{\omega}{r^3} d\xi$$

$$I_x = \int_0^{X_b} [A - B(t - t_b)] \frac{x - \xi}{r^3} d\xi$$

For supersonic penetrators, these equations apply to derivatives of the first integral in Equation 5.

The integrals I_{ω} and I_x must be evaluated at each time step. In Reference 13, fluid properties were calculated at a sequence of time steps. The numerical approach was then to calculate time derivatives $\partial I_{\omega}/\partial t$ and $\partial I_x/\partial t$, which were then numerically integrated. Analytical expressions for these time derivatives were derived as

$$\frac{\partial I_{\omega}}{\partial t} = \left(A_b - B \frac{R_b}{c} \right) \frac{\omega}{R_b^3} \frac{V_b}{1 - \frac{V_b}{c} \frac{x - X_b}{R_b}} - \frac{B}{\omega} \left(\frac{x}{R_o} - \frac{x - X_b}{R_b} \right) \quad (12)$$

and

$$\frac{\partial I_x}{\partial t} = \left(A_b - B \frac{R_b}{c} \right) \frac{x - X_b}{R_b^3} \frac{V_b}{1 - \frac{V_b}{c} \frac{x - X_b}{R_b}} + B \left(\frac{1}{R_o} - \frac{1}{R_b} \right) \quad (13)$$

This approach loses accuracy when the integration time step is large or the penetrator velocity is close to sonic. A more satisfactory approach is to calculate the integrals I_{ω} and I_x as functions of X_b instead of time t . From the chain rule of differentiation, one gets

$$\frac{\partial I}{\partial t} = \frac{\partial I}{\partial X_b} \frac{\partial X_b}{\partial t} \quad (14)$$

and from Reference 13 the derivative

$$\frac{\partial X_b}{\partial t} = \frac{V_b}{1 - \frac{V_b}{c} \left(\frac{x - X_b}{R_b} \right)} \quad (15)$$

Solving for $\partial I/\partial X_b$ and substituting Equations 12 or 13 and Equation 15, one gets

$$\frac{\partial I_\omega}{\partial X_b} = \left(A_b - B \frac{R_b}{c} \right) \frac{\omega}{R_b^3} - \frac{1 - \frac{V_b}{c} \left(\frac{x - X_b}{R_b} \right)}{V_b} B \left(\frac{x}{R_o} - \frac{x - X_b}{R_b} \right) \quad (16)$$

and

$$\frac{\partial I_x}{\partial X_b} = \left(A_b - B \frac{R_b}{c} \right) \left(\frac{x - X_b}{R_b^3} \right) + \frac{1 - \frac{V_b}{c} \left(\frac{x - X_b}{R_b} \right)}{V_b} B \left(\frac{1}{R_o} - \frac{1}{R_b} \right) \quad (17)$$

Equations 16 and 17 are numerically integrated to obtain $I_\omega(X_b)$ and $I_x(X_b)$. In order to get $I_\omega(t)$ and $I_x(t)$ required for Equations 10 and 11, one uses

$$t = t_b + \frac{1}{c} \sqrt{(x - X_b)^2 + \omega^2} \quad (18)$$

In Equations 9, 10, and 11 a singularity occurs when

$$V_b \frac{x - X_b}{R_b} = c \quad (19)$$

As shown in Figure 4, the left-hand side is the component of penetrator velocity along a line connecting the projectile and the observer at (x, ω) . The singularity occurs when this velocity is sonic. According to Equation 19 the singularity occurs only in the forward hemisphere from the projectile. In the computer program based on this analysis, the singularity was artificially removed by imposing the limit

$$\left| 1 - \frac{V_b}{c} \left(\frac{x - X_b}{R_b} \right) \right| > 0.1 \quad (20)$$

When this analysis was initiated for supersonic projectiles it was thought that the singularity arising from the first integral in Equation 5 might be canceled by the second integral in Equation 5 because of their opposite signs. This turned out not to be the case.

Pressure waves reflected from fuel cell walls have a significant effect on the fluid pressure distribution. In Reference 3 it was shown that the typically light construction of aircraft fuel cell walls produces wave reflections as if the walls were free surfaces. Since the flow is described by a potential, the wave reflections can be calculated using the method of images. The computer program described in Reference 13 uses an array of images to calculate the wave reflections from walls of rectangular volumes. The surfaces must be either free

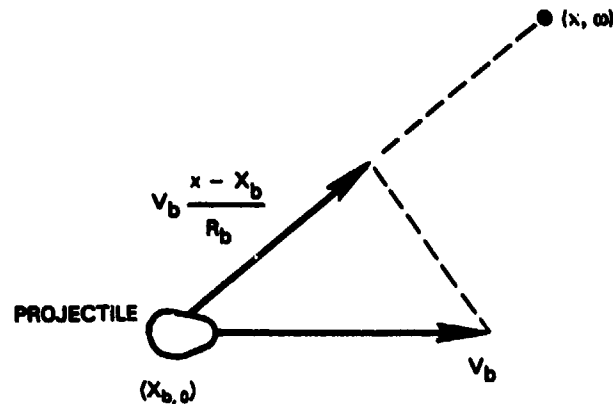


FIGURE 4. Geometry Showing Velocity Components for Sonic Singularity.

surfaces (using negative images) or rigid surfaces (using positive images). The surfaces must all be of one type or the other. The computer program based on this analysis has a slightly enhanced capability. Each wall may be individually chosen free or rigid.

FLUID/STRUCTURE INTERACTION

The analytical prediction of hydraulic ram structural effects is complicated by the fact that motion of the structure generates a pressure within the fluid. The strength of the interaction depends on the fluid density and is very important in hydraulic ram, whereas it can be neglected in most air blast problems since the air density is comparatively low.

The fluid pressure acting on the fluid/structure interface can be decomposed into incident and reflected pressure waves. The incident wave arises from action of the ballistic penetrator and may include wave reflections from other wall surfaces of the tank. The incident wave is independent of the motion of the fluid/structure interface. It is calculated using equations given in the Pressure Wave Generation section. The reflected pressure wave depends both on the incident wave and the motion of the fluid/structure interface. To calculate the reflected wave involves the solution of a diffraction problem. The formal solution is known and requires the evaluation of Kirkoff's integral (Reference 3). Because the approach is computationally laborious, several approximate solution methods have been applied.

The variable image method derived in Reference 11 is used here. It is extended to more general interface boundary conditions so that more complex fuel tank wall constructions can be examined.

Following Reference 11, the pressure field in the fuel cell is described by a potential ϕ that satisfies the wave equation. The pressure is given by Bernoulli's equation

$$P = -\rho \frac{\partial \phi}{\partial t} - \frac{1}{2} \rho u^2 \quad (21)$$

and the fluid particle velocity by

$$u = \nabla \phi \quad (22)$$

The fluid density is denoted by ρ . In most cases, the dynamic pressure, $1/2 \rho u^2$, in Bernoulli's equation is small and will be neglected here.

Let the potential of the incident wave be ϕ_i and write the potential of the reflected wave as

$$\phi_r = Q \tilde{\phi}_i \quad (23)$$

where $\tilde{\phi}_i$ is the mirror image of ϕ_i about the plane of the wall. In general, Q varies in space and time such that ϕ_r satisfies the wave equation. The pressure of the reflected wave is given by

$$P_r = -\rho \frac{\partial \phi_r}{\partial t} = -\rho Q \frac{\partial \tilde{\phi}_i}{\partial t} - \rho \tilde{\phi}_i \frac{\partial Q}{\partial t} \quad (24)$$

and the normal component of the fluid velocity is

$$u_{rn} = \frac{\partial \phi_r}{\partial n} = Q \frac{\partial \tilde{\phi}_i}{\partial n} + \tilde{\phi}_i \frac{\partial Q}{\partial n} \quad (25)$$

At the fluid/structure interface one has

$$\begin{aligned} \tilde{\phi}_i &= \phi_i \\ \frac{\partial \tilde{\phi}_i}{\partial t} &= \frac{\partial \phi_i}{\partial t} \\ \frac{\partial \tilde{\phi}_i}{\partial n} &= -\frac{\partial \phi_i}{\partial n} \end{aligned} \quad (26)$$

Substituting Equations 26 into 24 and 25, and using Equations 21 and 22 for the potential derivatives, one gets, respectively,

$$\begin{aligned} P_r &= QP_i - \rho\phi_i \frac{\partial Q}{\partial t} \\ u_{rn} &= -Qu_{in} + \phi_i \frac{\partial Q}{\partial n} \end{aligned} \quad (27)$$

In Reference 11, the assumption is made that

$$\frac{\partial Q}{\partial n} = \frac{1}{c} \frac{\partial Q}{\partial t} \quad (28)$$

on the fluid/structure interface and Equation 27 becomes

$$\begin{aligned} P_r &= QP_i - \rho\phi_i \frac{\partial Q}{\partial t} \\ u_{rn} &= -Qu_{in} + \frac{\phi_i}{c} \frac{\partial Q}{\partial t} \end{aligned} \quad (29)$$

The total interface pressure (P) and normal fluid velocity (u_n) are

$$\begin{aligned} P &= P_i + P_r = (1 + Q)P_i - \rho\phi_i \frac{\partial Q}{\partial t} \\ u_n &= u_{ni} + u_{nr} = (1 - Q)u_{ni} + \frac{\phi_i}{c} \frac{\partial Q}{\partial t} \end{aligned} \quad (30)$$

The assumption expressed by Equation 28 produces exact results for several cases of interest. When Q is constant, Equation 30 is valid for rigid surfaces ($Q = 1$), free surfaces ($Q = -1$), and transmissive surfaces ($Q = 0$).

In Reference 11, it was assumed that the fluid was in contact with the wall, and so the wall velocity (u_w) equals the normal fluid velocity. Under these conditions, Equation 30 can be recast as

$$P = (1 + Q)P_i + \rho c[(1 - Q)u_{ni} - u_w] \quad (31)$$

$$\frac{dQ}{dt} = -\frac{c}{\phi_i} [(1 - Q)u_{ni} - u_w] \quad (32)$$

Equation 31 relates the total wall pressure (P) to the wall motion (u_w) with Q as a parameter. To find Q, the differential Equation 31 is numerically integrated together with the equations

of motion of the wall. Equations 31 and 32 are used for the fluid/structure interaction in the HRSR computer program (Reference 16).

The initial value of $Q = 1$ is chosen in order for Equation 31 to give the correct pressure doubling effect. A difficulty with Equation 32 arises because initially $\phi = 0$ and $u_w = 0$ and is therefore indeterminate. In References 11 and 16, this indeterminacy was removed by setting the initial value of ϕ to a small positive value.

A second difficulty with Equation 32 arises when the wall begins to move before the incident wave arrives. Under this circumstance, $u_w \neq 0$ and $\phi = 0$, making Equation 32 singular. In Reference 16 the approach chosen was to set $Q = 1$ before the incident wave arrives, then use Equation 32 thereafter.

In general, the fluid does not remain in contact with the fuel cell walls. Large negative pressures are often developed at the wall, which can lead to fluid cavitation. Equations 31 and 32 do not apply in this situation. The approach to cavitation taken in Reference 16 was simply to truncate the total wall pressure at zero.

Cavitation is one example of a pressure-dependent boundary condition. Another example occurs when a layer of crushable foam is used to isolate the tank structure from hydraulic ram pressure loading. For the analysis of these cases, Equation 30 can be written as

$$u_n = (1 - Q)u_{ni} + \frac{1}{\rho c} [(1 + Q)P_i - P] \quad (33)$$

$$\frac{dQ}{dt} = \frac{1}{\rho \phi_i} [(1 + Q)P_i - P] \quad (34)$$

In Equation 34, P may be a constant, as in the case of cavitation, or may be a prescribed function of foam thickness. Given the value of Q by integration of Equation 34, the fluid surface velocity is then calculated from Equation 33. For either cavitation or foam layers, the distance between the fluid surface and the wall must be known. The fluid surface position is calculated by integrating Equation 33.

STRUCTURAL RESPONSE MODELS

LAGRANGIAN FORMULATION

The structural response models are derived using the Lagrange equations of motion. In this method, the panel deflection profile and strain distribution are postulated *a priori* as simple functions over the panel surface. The functions contain one or more parameters that may vary with time. These parameters are the generalized coordinates of the Lagrangian theory and are obtained by solving the Lagrangian differential equations of motion.

NWC TP 6770

The Lagrangian, L , is defined in terms of the kinetic energy, T , and potential energy, V , of the panel as

$$L = T(q, \dot{q}) - V(q) \quad (35)$$

where q is a vector of generalized coordinates having components q_k . The vector, \dot{q} , is the time derivative of q .

The Lagrangian equations of motion are given by

$$\frac{d}{dt} \left(\frac{\partial L}{\partial \dot{q}_k} \right) - \frac{\partial L}{\partial q_k} = Q_k \quad (36)$$

or, substituting Equation 35 for L ,

$$\frac{d}{dt} \left(\frac{\partial T}{\partial \dot{q}_k} \right) = \frac{\partial T}{\partial q_k} - \frac{\partial V}{\partial q_k} + Q_k \quad (37)$$

The panel motion is described in terms of the deflection w , normal to the panel

$$w = w(q, x, y) \quad (38)$$

where x and y are coordinates spanning the panel. In-plane displacements are given by u and v in x and y directions,

$$u = u(q, x, y) \quad (39)$$

$$v = v(q, x, y) \quad (40)$$

The kinetic energy of the panel is given by the integral

$$T = \frac{\gamma h}{2} \iint \left(\frac{\partial w}{\partial t} \right)^2 dx dy \quad (41)$$

where γ is the mass density of the panel material and h is the panel thickness. The integral extends over the surface of the panel. The kinetic energy of the in-plane displacements is neglected.

The generalized force acting on the panel is given by the integral

$$Q_k = \iint P \frac{\partial w}{\partial q_k} dx dy \quad (42)$$

where P is the hydrostatic pressure acting normal to the panel. In-plane components of the pressure loading acting during large deflections are neglected.

NWC TP 6770

The potential energy of the panel is partitioned into bending and membrane strain energy contributions. Stress-strain relations for orthotropic plates (Reference 13) are

$$\begin{aligned} \sigma_x &= E'_x \epsilon_x + E'' \epsilon_y \\ \sigma_y &= E'_y \epsilon_y + E'' \epsilon_x \\ \tau_{xy} &= G \gamma_{xy} \end{aligned} \quad (43)$$

where σ_x and σ_y are stress components, τ_{xy} is shear stress, ϵ_x and ϵ_y are strain components, and γ_{xy} is shear strain. The four constants E'_x , E'_y , E'' , and G are needed to characterize the orthotropic panels. For the particular case of isotropic materials we have

$$\begin{aligned} E'_x &= E'_y = \frac{E}{1 - \nu^2} \\ G &= \frac{E}{2(1 + \nu)} \quad E'' = \frac{\nu E}{1 - \nu^2} \end{aligned} \quad (44)$$

where E is Young's modulus and ν is Poisson's ratio.

For pure bending, the strain components are given by

$$\begin{aligned} \epsilon_x &= -z \frac{\partial^2 w}{\partial x^2} \\ \epsilon_y &= -z \frac{\partial^2 w}{\partial y^2} \\ \gamma_{xy} &= -2z \frac{\partial^2 w}{\partial x \partial y} \end{aligned} \quad (45)$$

where z is the distance from the panel. Expressions for bending moments, M_x and M_y , and the twisting moment, M_{xy} , for a plate of thickness h are

$$\begin{aligned} M_x &= \int_{-h/2}^{h/2} \sigma_x z dz = -D_x \frac{\partial^2 w}{\partial x^2} - D_1 \frac{\partial^2 w}{\partial y^2} \\ M_y &= \int_{-h/2}^{h/2} \sigma_y z dz = -D_y \frac{\partial^2 w}{\partial y^2} - D_1 \frac{\partial^2 w}{\partial x^2} \\ M_{xy} &= - \int_{-h/2}^{h/2} \tau_{xy} z dz = 2D_{xy} \frac{\partial^2 w}{\partial x \partial y} \end{aligned} \quad (46)$$

where the bending coefficients are given by

$$\begin{aligned} D_x &= \frac{E_x' h^3}{12}, \quad D_y = \frac{E_y' h^3}{12} \\ D_1 &= \frac{K' h^3}{12}, \quad D_{xy} = \frac{G' h^3}{12} \end{aligned} \quad (47)$$

Following Reference 13, the bending strain energy of an orthotropic plate element is given by

$$dV_b = -\frac{1}{2} \left(M_x \frac{\partial^2 w}{\partial x^2} + M_y \frac{\partial^2 w}{\partial y^2} + M_{xy} \frac{\partial^2 w}{\partial x \partial y} \right) dx dy \quad (48)$$

Substituting Equation 46 for the bending moments and integrating gives

$$\begin{aligned} V_b &= \frac{1}{2} \int \int \left\{ D_x \left(\frac{\partial^2 w}{\partial x^2} \right)^2 + 2D_1 \frac{\partial^2 w}{\partial x^2} \frac{\partial^2 w}{\partial y^2} \right. \\ &\quad \left. + D_y \left(\frac{\partial^2 w}{\partial y^2} \right)^2 + 4D_{xy} \left(\frac{\partial^2 w}{\partial x \partial y} \right)^2 \right\} dx dy \end{aligned} \quad (49)$$

The membrane strain energy of an orthotropic plate element is given by

$$V_m = \frac{1}{2} h \int \int \left\{ \epsilon_x \sigma_x + \epsilon_y \sigma_y + \gamma_{xy} \tau_{xy} \right\} dx dy \quad (50)$$

For large deflections, the strains are given

$$\begin{aligned} \epsilon_x &= \frac{\partial u}{\partial x} + \frac{1}{2} \left(\frac{\partial w}{\partial x} \right)^2 \\ \epsilon_y &= \frac{\partial v}{\partial y} + \frac{1}{2} \left(\frac{\partial w}{\partial y} \right)^2 \\ \gamma_{xy} &= \frac{\partial u}{\partial y} + \frac{\partial v}{\partial x} + \frac{\partial w}{\partial x} \frac{\partial w}{\partial y} \end{aligned} \quad (51)$$

Substituting Equations 43 and 51 into 50 and expanding the result yields

$$\begin{aligned}
 V_m = \frac{h}{2} \int \int \left\{ \right. & E_x \left[u_x^2 + u_x w_x^2 + \frac{1}{4} w_x^4 \right] \\
 & + E_y \left[v_y^2 + v_y w_y^2 + \frac{1}{4} w_y^4 \right] \\
 & + E'' \left[2u_x v_y + u_x w_y^2 + v_y w_x^2 + \frac{1}{2} w_x^2 w_y^2 \right] \\
 & + G_{xy} \left[u_y^2 + v_x^2 + 2u_y v_x + 2u_y w_x w_y \right. \\
 & \left. \left. + 2v_x w_x w_y + w_x^2 w_y^2 \right] \right\} dx dy
 \end{aligned} \tag{52}$$

The subscript notation is used for the partial derivatives of u , v , and w .

DISPLACEMENT FUNCTIONS

There are several possibilities for the displacement functions (Equations 38, 39, and 40). In Reference 11, the equations were applied to an isotropic rectangular panel with dimensions a and b . The displacement functions used are

$$\begin{aligned}
 w &= w_0 \cos X \cos Y \\
 u &= c \sin 2X \cos Y \\
 v &= c \cos X \sin 2Y
 \end{aligned} \tag{53}$$

where the arguments X and Y are given by

$$X = \frac{\pi x}{a}, \quad Y = \frac{\pi y}{b}$$

The origin of x and y are in the center of the panel. The amplitudes w_0 and c are identified as the generalized coordinates q in Equations 38, 39, and 40. The Lagrangian Equation 37 is integrated to obtain w_0 and c as a function of time. In Reference 11, the structural model was restricted to isotropic panels. When comparing the computed $w_0(t)$ to the results of a hydraulic ram exit panel test, agreement was quite reasonable.

The equations for the more general case of orthotropic materials were developed in Reference 15. The displacement functions (Equation 53) were used. Predictions of panel stress were made for impact walls of hydraulic ram tests. Agreement was so poor that the technique was abandoned for several years.

The Lagrangian equations described here give a satisfactory approximation to the panel motion only when the assumed displacement functions resemble the actual panel displacement. In the exit wall shot of Reference 11, Equation 53 was adequate to show reasonable agreement with wall deflection. However, this does not imply that the calculation of stress will give similarly good agreement. The shots in Reference 15 were performed on entrance panels that are expected to have a more highly concentrated pressure loading than exit wall shots and therefore a different wall displacement. Also, the entrance panels in Reference 15 were mounted in a frame that allowed in-plane motion at the panel edges. This boundary condition is not satisfied by Equation 53, which assumes clamped edges.

The value of the Lagrangian technique is the speedy solution of the structural response equations compared to a finite element solution. The drawback is the inaccuracy obtained when the postulated displacement functions do not adequately approximate the actual panel motion. Three different sets of displacement functions are included here so that one may choose the most appropriate for a given structural configuration and shotline geometry.

The displacement functions used in Reference 11 are generalized slightly to

$$\begin{aligned}w &= w_0 \cos X \cos Y \\u &= u_0 \sin 2X \cos Y \\v &= v_0 \cos X \sin 2Y\end{aligned}\tag{54}$$

where, again,

$$X = \frac{\pi x}{a}, \quad Y = \frac{\pi y}{b}.$$

The amplitudes u_0 and v_0 are allowed to vary independently to give, hopefully, a more accurate result. Equation 54 should be used when panels have fixed boundaries and panel motion resembling the first mode is anticipated. This set of functions will be referred to as the fixed-boundary displacements.

The test fixture used in Reference 15 inspired the second test of displacement functions

$$\begin{aligned}w &= w_0 \cos X \cos Y \\u &= u_0 \sin X \cos Y + \frac{\pi}{4a} w_0^2 \sin 2X \cos^2 Y\end{aligned}$$

$$v = v_0 \cos Y \sin X + \frac{n}{4b} \omega_0^2 \cos^2 X \sin 2Y \quad (55)$$

where, again,

$$X = \frac{\pi x}{a}, \quad Y = \frac{\pi y}{b}.$$

The second term in the expressions for in-plane displacements (u and v) is included to make the normal stresses vanish at the panel edges. Since the normal stresses vanish, this set of displacement functions will be referred to as the free-boundary displacements.

Neither the fixed nor the free displacement functions are appropriate for large panels or for the initial stages of the entrance panel problem. Here, a Gaussian set of displacement functions is defined by

$$\begin{aligned} w &= w_0 e^{-(X^2 + Y^2)} \\ u &= S_{ux}x + S_{uy}y + u_0 X e^{-(X^2 + Y^2)} \\ v &= S_{vx}x + S_{vy}y + v_0 Y e^{-(X^2 + Y^2)} \end{aligned} \quad (56)$$

where

$$X = \frac{x - x_0}{a}, \quad Y = \frac{y - y_0}{b}$$

The constants S_{ux} , S_{uy} , S_{vx} , and S_{vy} determine an initial uniform stress loading applied to the panel. The Gaussian amplitudes (w_0 , u_0 , v_0), as well as the Gaussian widths and centers (a , b , x_0 , and y_0) are all generalized coordinates satisfying the Lagrange differential equations.

EVALUATION OF ENERGY INTEGRALS

The integrals for kinetic energy and strain energy need to be evaluated. This procedure is straightforward but very tedious. The kinetic energy integral (Equation 41) yields the same result for both cosine law displacement functions (Equations 54 and 55)

$$T = \frac{\gamma h a b}{8} \dot{w}_0^2 \quad (57)$$

where the dot denotes differentiation with respect to time.

The Gaussian displacement functions (Equation 56) give a more complicated result since the generalized coordinates a , b , x_0 , and y_0 are all functions of time. Substituting

Equation 56 into the kinetic energy integral (Equation 41), then integrating over an infinite panel, one gets

$$T = \frac{\pi \gamma h a b}{4} \left[\dot{w}_0^2 + \frac{3}{4} w_0^2 \frac{\dot{a}^2}{a^2} + \frac{3}{4} w_0^2 \frac{\dot{b}^2}{b^2} + w_0^2 \frac{\dot{x}_0^2}{a^2} + w_0^2 \frac{\dot{y}_0^2}{b^2} + w_0 \dot{w}_0 \frac{\dot{a}}{a} + w_0 \dot{w}_0 \frac{\dot{b}}{b} + \frac{1}{2} w_0^2 \frac{\dot{a} \dot{b}}{a b} \right] \quad (58)$$

The bending strain integral (Equation 49) also gives the same result for both sets of cosine law displacement functions. Substituting either Equation 54 or Equation 55 into Equation 49 and integrating over the plate area gives the result

$$V_b = \frac{\pi}{16} a b w_0^2 \left(\frac{D_x}{a^4} + \frac{2D_1}{a^2 b^2} + \frac{D_y}{b^4} + \frac{4D_{xy}}{a^2 b^2} \right) \quad (59)$$

Similarly, substituting the Gaussian displacement functions of Equation 56 into Equation 49 and integrating over an infinite plate area one gets

$$V_b = \frac{3\pi}{16} a b w_0^2 \left(\frac{D_x}{a^4} + \frac{8D_1}{3a^2 b^2} + \frac{D_y}{b^4} + \frac{4D_{xy}}{3a^2 b^2} \right) \quad (60)$$

The membrane strain energy for the fixed boundary, cosine displacement function set is

$$V_m = \frac{1}{2} h a b \left[u_0^2 \pi^2 \left[\frac{K_x'}{a^2} + \frac{G_{xy}}{4b^2} \right] + u_0 v_0 \frac{32}{9ab} [K' + G_{xy}] + v_0^2 \pi^2 \left[\frac{K_y'}{b^2} + \frac{G_{xy}}{4a^2} \right] \right]$$

$$\begin{aligned}
 & -u_o \omega_o^2 \frac{2n^2}{3a} \left[\frac{E'_x}{a^2} - \frac{E''}{2b^2} + \frac{G_{xy}}{2b^2} \right] \\
 & -v_o \omega_o^2 \frac{2n^2}{3b} \left[\frac{E'_y}{b^2} - \frac{E''}{2a^2} + \frac{G_{xy}}{2a^2} \right] \\
 & + \omega_o^4 \frac{9n^4}{256} \left[\frac{E'_x}{a^4} + \frac{E'_y}{b^4} + \frac{2E''}{9a^2b^2} + \frac{4G_{xy}}{9a^2b^2} \right] \quad (61)
 \end{aligned}$$

For the free boundary displacement functions, the membrane strain energy integral is

$$\begin{aligned}
 V_m = \frac{hab}{2} \left\{ \right. \\
 & u_o^2 \frac{n^2}{4} \left(\frac{E'_x}{a^2} + \frac{G_{xy}}{b^2} \right) \\
 & + u_o v_o \frac{n^2}{2ab} (E'' + G_{xy}) \\
 & + v_o^2 \frac{n^2}{4} \left(\frac{E'_y}{b^2} + \frac{G_{xy}}{a^2} \right) \\
 & + u_o \omega_o^2 \frac{16n}{9a} \left(\frac{E'_x}{a^2} + \frac{E''}{b^2} \right) \\
 & + v_o \omega_o^2 \frac{16n}{9a} \left(\frac{E'_y}{b^2} + \frac{E''}{a^2} \right) \\
 & \left. + \omega_o^4 \frac{n^4}{256} \left(\frac{9E'_x}{a^4} + \frac{9E'_y}{b^4} + \frac{13E''}{a^2b^2} + \frac{12G_{xy}}{a^2b^2} \right) \right\} \quad (62)
 \end{aligned}$$

Finally, the membrane strain energy integral for the Gaussian displacement set is

$$\begin{aligned}
 V_m = \frac{\pi h a b}{2} & \left\{ \right. \\
 & \frac{1}{n} \left[S_{ux}^2 E'_x + S_{vy}^2 E'_y + 2 S_{ux} S_{vy} E'' \right. \\
 & \quad \left. + \left(S_{ux} + S_{vy} \right)^2 G_{xy} \right] \\
 & + u_o^2 \frac{1}{8\beta} \left[\frac{3E'_x}{a^2} + \frac{G_{xy}}{b^2} \right] \\
 & + u_o v_o \frac{1}{4ab\beta} \left[E'' + G_{xy} \right] \\
 & + v_o^2 \frac{12}{8\beta} \left[\frac{3E'_y}{b^2} + \frac{G_{xy}}{a^2} \right] \\
 & + u_o w_o^2 \frac{4}{ab^2(\beta+2)^3} \left[(\beta-1) \frac{b^2}{a^2} E'_x + E'' - \beta G_{xy} \right] \\
 & + v_o w_o^2 \frac{4}{ba^2(\beta+2)^3} \left[(\beta-1) \frac{a^2}{b^2} E'_y + E'' - \beta G_{xy} \right] \\
 & + w_o^2 \frac{1}{2} \left[\frac{E'_x S_{ux}}{a^2} + \frac{E'_y S_{vy}}{b^2} + \frac{E'' S_{vy}}{a^2} + \frac{E'' S_{ux}}{b^2} \right] \\
 & \left. + w_o^4 \frac{1}{64} \left[\frac{3E'_x}{a^4} + \frac{3E'_y}{b^4} + \frac{2E''}{a^2 b^2} + \frac{4G_{xy}}{a^2 b^2} \right] \right\} \quad (63)
 \end{aligned}$$

The Lagrange equation (Equation 37) can be simplified by noting that T , V_b , and Q_k are independent of the in-plane displacements u_o and v_o . For the case of Gaussian displacements, they are also independent of the parameter β . Therefore, for these variables, the Lagrange equations reduce to

$$\frac{\partial V_m}{\partial u_o} = \frac{\partial V_m}{\partial v_o} = \frac{\partial V_m}{\partial \beta} = 0 \quad (64)$$

The membrane energy V_m (Equations 61, 62, and 63) for the three displacement representations can be written in the quadratic form

$$\begin{aligned} V_m = & C_c + C_{uu} u_o^2 + C_{uv} u_o v_o + C_{vv} v_o^2 \\ & + C_{uw} u_o w_o^2 + C_{vw} v_o w_o^2 \\ & + C_{ww} w_o^2 + C_{ww} w_o^4 \end{aligned} \quad (65)$$

where the C 's are not functions of the u_o , v_o , or w_o , but may be functions of β for the Gaussian displacements.

If one differentiates Equation 65 according to Equation 64, one gets the system

$$\begin{aligned} 2C_{uu} u_o + C_{uv} v_o + C_{uw} w_o^2 &= 0 \\ C_{uv} u_o + 2C_{vv} v_o + C_{vw} w_o^2 &= 0 \end{aligned} \quad (66)$$

The solution of Equation 66 is

$$\begin{aligned} u_o &= C_u w_o^2 \\ v_o &= C_v w_o^2 \end{aligned}$$

where

$$\begin{aligned} C_u &= (C_{uv} C_{vw} - 2C_{vv} C_{uw}) / \Delta \\ C_v &= (C_{uv} C_{uw} - 2C_{uu} C_{vw}) / \Delta \end{aligned} \quad (68)$$

and the determinant, Δ , is given by

$$\Delta = 4C_{uu} C_{vv} - C_{uv}^2 \quad (69)$$

Thus, Equation 67 gives u_o and v_o when w_o , a , and b are known (since the C 's are functions of a and b).

For Gaussian displacements, the C_u and C_v are functions of the parameter β . At this point in the development, the last of Equation 64 is still not satisfied. The variation of membrane energy with β is shown in Figure 5. The curves in Figure 5 result from Equation 62 applied to an isotropic panel with $a = b$ and $S_{ux} = S_{vx} = S_{uy} = S_{vy} = 0$. Curves are plotted in Figure 5 for values of Poisson's ratio of 0.25 to 0.35, which covers the range of interest. All of the curves show a broad minimum at around $\beta = 3$. This value is fixed for all future analysis. The other minimum in Figure 5, with $\beta < 1$, corresponds to a compressive membrane stress at the Gaussian center and is therefore not a good choice.

The distribution of membrane strain over the panel is given in Equation 51 as a function of derivatives of displacements. The membrane strains are calculated and plotted in Figures 6 through 9 as a function of distance along the x axis from the panel center. Along this line the components of membrane strain ϵ_x and ϵ_y in Equation 51 are labeled radial and hoop strain in the figures. The membrane strains are normalized for an isotropic square panel with a Poisson's ratio of 0.3.

Profiles of the radial and hoop components of the normalized membrane strain are plotted in Figures 6 and 7 for the Gaussian displacements. The strains are plotted for several values of the parameter α in order to show its effect. The curves corresponding to $\alpha = 3$, which was chosen on the basis of minimum energy, appear to be the most physically realistic.

Profiles of membrane strain for cosine deflections are plotted in Figures 8 and 9 for fixed and free boundary conditions, respectively.

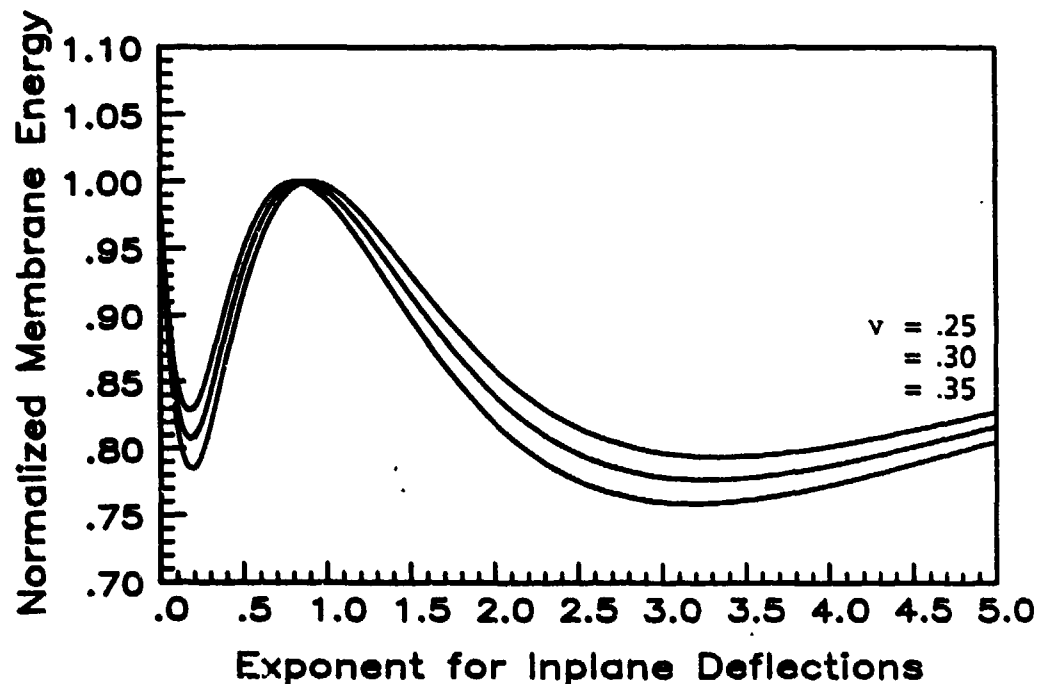


FIGURE 5. Normalized Membrane Energy (Equation 63) for Gaussian Displacements of Isotropic Square Panels as a Function of the Parameter β , Which is Defined by Equation 56.

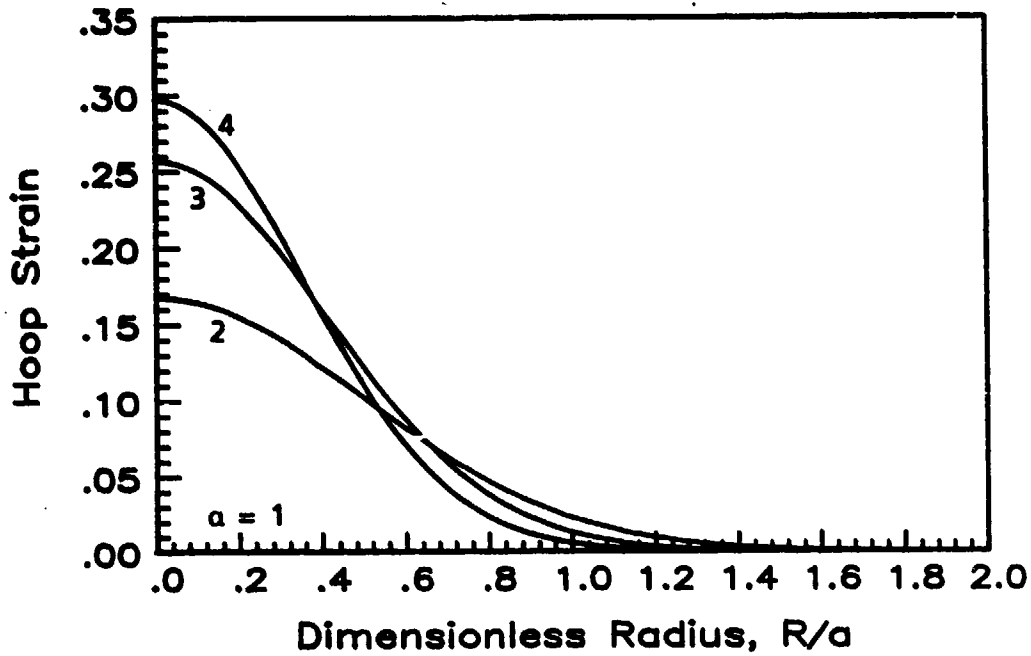


FIGURE 6. Normalized Membrane Radial Strain Distribution in Isotropic Square Panels for Gaussian Deflections Showing the Effect of the Parameter β .

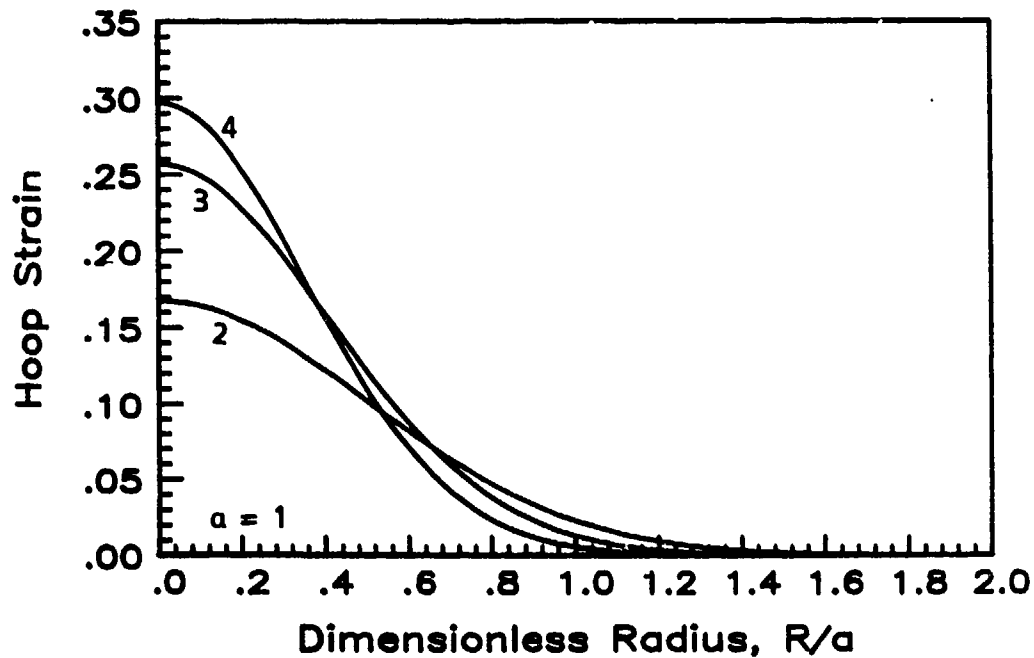


FIGURE 7. Normalized Membrane Hoop Strain Distribution in Isotropic Square Panels for Gaussian Deflections Showing the Effect of the Parameter β .

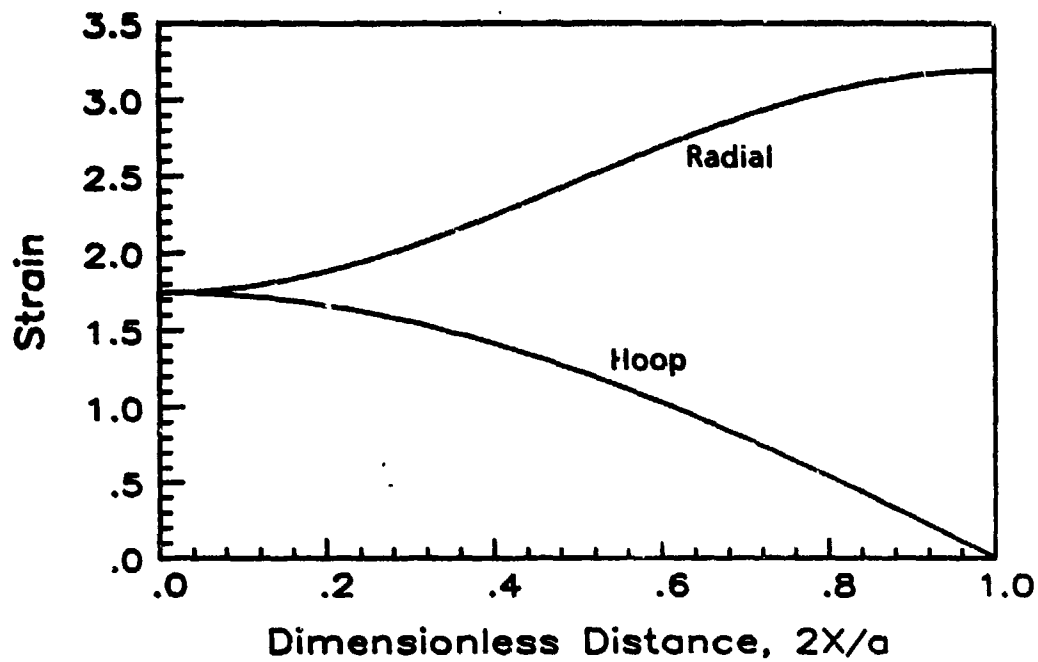


FIGURE 8. Normalized Radial and Hoop Membrane Strain for Cosine Deflections (Equation 54) of an Isotropic Square Panel With Fixed Boundary Conditions.

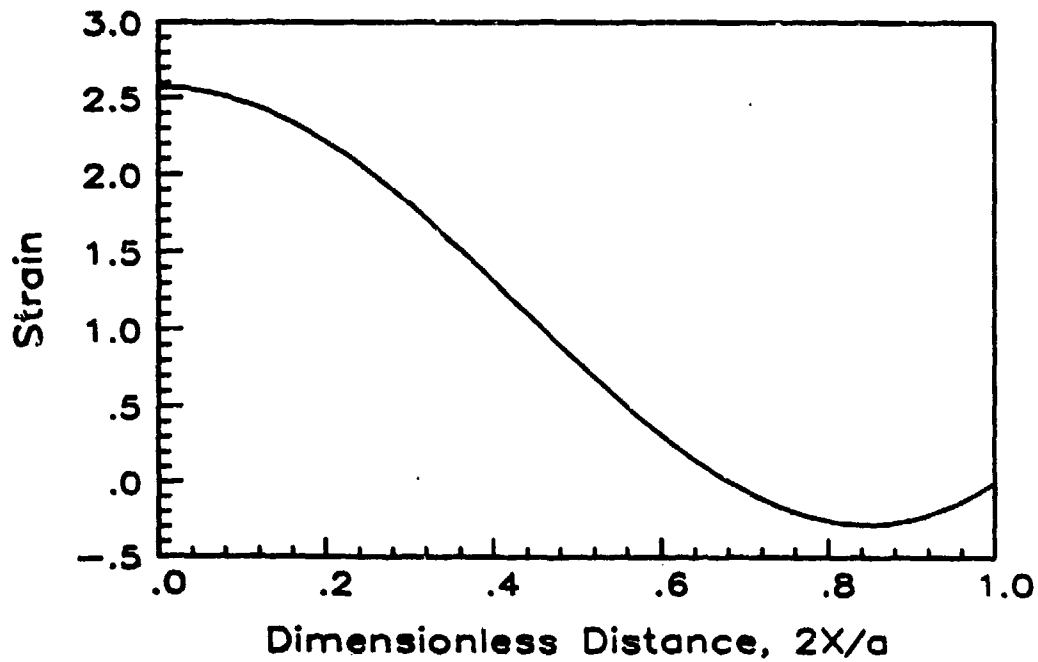


FIGURE 9. Normalized Radial Strain for Cosine Deflections (Equation 55) of an Isotropic Square Panel With Free Boundary Conditions.

EQUATIONS OF MOTION FOR COSINE DEFLECTIONS

For the cosine deflection functions with either fixed or free edges, the only remaining generalized coordinate is w_o . To evaluate the Lagrange equation (Equation 37), first rewrite the kinetic energy integral (Equation 57) as

$$T = \frac{1}{2} C_p \dot{w}_o^2 \quad (70)$$

where

$$C_p = \frac{\gamma h a b}{4} \quad (71)$$

The various derivatives of the kinetic energy integral required for Equation 37 are

$$\frac{\partial T}{\partial \dot{w}_o} = C_p \dot{w}_o$$

$$\frac{d}{dt} \left(\frac{\partial T}{\partial \dot{w}_o} \right) = C_p \ddot{w}_o \quad (72)$$

$$\frac{\partial T}{\partial w_o} = 0 \quad (73)$$

Similarly, the bending strain energy (Equation 59) can be expressed as

$$V_b = \frac{1}{2} C_b w_o^2 \quad (74)$$

where

$$C_b = \frac{\pi}{8} a b \left(\frac{D_x}{a^4} + \frac{2D_1}{a^2 b^2} + \frac{D_y}{b^4} + \frac{4D_{xy}}{a^2 b^2} \right) \quad (75)$$

whence, the required derivative is

$$\frac{\partial V_b}{\partial w_o} = C_b w_o \quad (76)$$

The derivative of the membrane strain energy is obtained from Equation 65

$$\frac{\partial V_m}{\partial w_o} = 2C_{uw} u_o w_o + 2C_{vw} v_o w_o^2 + 4C_{ww} w_o^3 \quad (77)$$

For the cosine deflections, the C_w term vanishes, so it was not included in Equation 77.

The u_o and v_o in Equation 77 can be eliminated using Equation 67, whence

$$\frac{\partial V_m}{\partial w_o} = C_m w_o^3 \quad (78)$$

where

$$C_m = 2C_{uw} C_u + 2C_{vw} C_v + 4C_{ww} \quad (79)$$

Substituting the derivatives of Equations 72, 73, 76, and 78 into Equation 78, one obtains

$$C_p \ddot{w}_o + C_b w_o + C_m w_o^3 = Q_{w_o} \quad (80)$$

The generalized force acting on the panel must be evaluated numerically. For the cosine deflections it is

$$Q_{w_o} = \iint P \cos X \cos Y \, dx dy \quad (81)$$

where the integral is taken over the area of the panel. The second-order differential equation for w_o may be solved by a variety of techniques when the pressure P is known.

EQUATIONS OF MOTION FOR GAUSSIAN DEFLECTIONS

The Lagrangian equation (Equation 37) for the Gaussian deflections is more complex because there are more independent generalized coordinates. The in-plane deflection equations have already been integrated, resulting in Equation 67. There remains the out-of-plane deflection (w_o), the Gaussian widths (a and b), and the Gaussian centers (x_o and y_o). Therefore, five Lagrangian equations are required.

The total time derivative in Equation 37 is expanded in the usual way with the chain rule for differentiation

$$\begin{aligned} \frac{d}{dt} \left(\frac{\partial T}{\partial \dot{q}} \right) = & \left(\ddot{w}_o \frac{\partial}{\partial \dot{w}_o} + \ddot{a} \frac{\partial}{\partial \dot{a}} + \ddot{b} \frac{\partial}{\partial \dot{b}} + \ddot{x}_o \frac{\partial}{\partial \dot{x}_o} \right) \\ & + \ddot{y}_o \frac{\partial}{\partial \dot{y}_o} + \dot{w}_o \frac{\partial}{\partial w_o} + \dot{a} \frac{\partial}{\partial a} + \dot{b} \frac{\partial}{\partial b} \\ & + \dot{x}_o \frac{\partial}{\partial x_o} + \dot{y}_o \frac{\partial}{\partial y_o} \left) \frac{\partial T}{\partial \dot{q}} \end{aligned} \quad (82)$$

The q in Equation 82 can be any of the five generalized coordinates. The derivatives with respect to the various \dot{q} are

$$\begin{aligned} \frac{\partial T}{\partial \dot{w}_o} &= \frac{\gamma h \pi}{4} \left[2ab\dot{w}_o + w_o b\dot{a} + w_o a\dot{b} \right] \\ \frac{\partial T}{\partial \dot{a}} &= \frac{\pi \gamma h}{4} \left[w_o b\dot{w}_o + \frac{3}{2} w_o^2 b \frac{\dot{a}}{a} + \frac{1}{2} w_o^2 \dot{b} \right] \\ \frac{\partial T}{\partial \dot{b}} &= \frac{\pi \gamma h}{4} \left[w_o a\dot{w}_o + \frac{1}{2} w_o^2 \dot{a} + \frac{3}{2} w_o^2 a \frac{\dot{b}}{b} \right] \\ \frac{\partial T}{\partial \dot{x}_o} &= \frac{\pi \gamma h}{4} \left[2w_o^2 \frac{b}{a} \dot{x}_o \right] \\ \frac{\partial T}{\partial \dot{y}_o} &= \frac{\pi \gamma h}{4} \left[2w_o^2 \frac{a}{b} \dot{y}_o \right] \end{aligned} \quad (83)$$

The various kinetic energy derivatives required for the Lagrangian equations are obtained by substituting the five partial derivatives, Equations 83, into 82, with the results

$$\begin{aligned} \frac{d}{dt} \left(\frac{\partial T}{\partial \dot{w}_o} \right) &= \frac{\gamma h \pi}{4} \left\{ 2ab\ddot{w}_o + w_o b\ddot{a} + w_o a\ddot{b} \right. \\ &\quad \left. + 3\dot{a}\dot{b}\dot{w}_o + 3a\dot{b}\dot{w}_o + 2w_o \dot{a}\dot{b} \right\} \\ \frac{d}{dt} \left(\frac{\partial T}{\partial \dot{a}} \right) &= \frac{\gamma h \pi}{4} \left\{ w_o b\ddot{w}_o + \frac{3}{2} w_o^2 \frac{b}{a} \ddot{a} + \frac{1}{2} w_o^2 \ddot{b} \right. \\ &\quad \left. + 2w_o \dot{b}\dot{w}_o + b\dot{w}_o^2 - \frac{3}{2} w_o^2 \frac{b}{a^2} \dot{a}^2 \right. \\ &\quad \left. + 3w_o \frac{b}{a} \dot{w}_o \dot{a} + \frac{3}{2} w_o^2 \frac{1}{a} \dot{a}\dot{b} \right\} \end{aligned}$$

$$\begin{aligned}
 \frac{d}{dt} \left(\frac{\partial T}{\partial \dot{b}} \right) &= \frac{\gamma \hbar n}{4} \left\{ \omega_o a \ddot{w}_o + \frac{1}{2} \omega_o^2 \ddot{a} + \frac{3}{2} \omega_o^2 \frac{a}{b} \ddot{b} \right. \\
 &\quad + 2 \omega_o \dot{a} \dot{w}_o + a \dot{w}_o^2 - \frac{3}{2} \omega_o^2 \frac{a}{b^2} \dot{b}^2 \\
 &\quad \left. + 3 \omega_o \frac{a}{b} \dot{w}_o \dot{b} + \frac{3}{2} \omega_o^2 \frac{1}{b} \dot{a} \dot{b} \right\} \\
 \frac{d}{dt} \left(\frac{\partial T}{\partial \dot{x}_o} \right) &= \frac{\gamma \hbar n}{4} \left\{ 2 \omega_o^2 \frac{b}{a} \ddot{x}_o + \omega_o \frac{b}{a} \dot{w}_o \dot{x}_o \right. \\
 &\quad \left. + 2 \omega_o^2 \frac{1}{a} \dot{b} \dot{x}_o - 2 \omega_o^2 \frac{b}{a^2} \dot{a} \dot{x}_o \right\} \\
 \frac{d}{dt} \left(\frac{\partial T}{\partial \dot{y}_o} \right) &= \frac{\gamma \hbar n}{4} \left\{ 2 \omega_o^2 \frac{a}{b} \ddot{y}_o + \omega_o \frac{a}{b} \dot{w}_o \dot{y}_o \right. \\
 &\quad \left. + 2 \omega_o^2 \frac{1}{b} \dot{a} \dot{y}_o - 2 \omega_o^2 \frac{a}{b^2} \dot{b} \dot{y}_o \right\}
 \end{aligned} \tag{84}$$

For brevity, we rewrite Equation 84 in the form

$$\begin{aligned}
 \frac{d}{dt} \left(\frac{\partial T}{\partial \dot{w}_o} \right) &= M_{11} \ddot{w}_o + M_{12} \ddot{a} + M_{13} \ddot{b} + A_1 \\
 \frac{d}{dt} \left(\frac{\partial T}{\partial \dot{a}} \right) &= M_{21} \ddot{w}_o + M_{22} \ddot{a} + M_{23} \ddot{b} + A_2 \\
 \frac{d}{dt} \left(\frac{\partial T}{\partial \dot{b}} \right) &= M_{31} \ddot{w}_o + M_{32} \ddot{a} + M_{33} \ddot{b} + A_3 \\
 \frac{d}{dt} \left(\frac{\partial T}{\partial \dot{x}_o} \right) &= M_{44} \ddot{x}_o + A_4 \\
 \frac{d}{dt} \left(\frac{\partial T}{\partial \dot{y}_o} \right) &= M_{55} \ddot{y}_o + A_5
 \end{aligned} \tag{85}$$

Therefore, the Lagrangian Equation 37 can be written as

$$\begin{aligned}
 M_{11}\ddot{w}_0 + M_{12}\ddot{a} + M_{13}\ddot{b} &= \frac{\partial T}{\partial \dot{w}_0} - \frac{\partial V_b}{\partial w_0} - \frac{\partial V_m}{\partial w_0} - A_1 + Q_{w_0} \\
 M_{21}\ddot{w}_0 + M_{22}\ddot{a} + M_{23}\ddot{b} &= \frac{\partial T}{\partial \dot{a}} - \frac{\partial V_b}{\partial a} - \frac{\partial V_m}{\partial a} - A_2 + Q_a \\
 M_{31}\ddot{w}_0 + M_{32}\ddot{a} + M_{33}\ddot{b} &= \frac{\partial T}{\partial \dot{b}} - \frac{\partial V_b}{\partial b} - \frac{\partial V_m}{\partial b} - A_3 + Q_b \\
 M_{44}\ddot{x}_0 &= -A_4 + Q_{x_0} \\
 M_{55}\ddot{y}_0 &= -A_5 + Q_{y_0}
 \end{aligned} \tag{86}$$

Vanishing terms were not included in Equation 86. The remaining derivatives are easy to derive, but are lengthy and will not be shown here. It should be noted that the derivatives of the membrane potential energy, V_m , are evaluated at constant u_0 and v_0 . These variables are then eliminated after the differentiation by using Equation 67.

The equations of motion (Equation 86) have the form of a mass matrix multiplying an acceleration on the left-hand side and a force on the right-hand side. The w_0 , a , and b accelerations are coupled. To integrate these equations, the accelerations must be solved for by inverting the mass matrix. This is done numerically. It should be noted that the mass matrix becomes singular when $w_0 = 0$, the initial condition. This can be rationalized by noting that the shape of the Gaussian is independent of the widths a and b when $w_0 = 0$; it vanishes everywhere.

EXPERIMENT

Hydraulic ram testing was performed to obtain data for comparison with the analysis. The target test tank was a 2-foot cube filled with water. Projectiles were steel right cylinders; they were 0.5 inch diameter, 1.5 inch long, and weighed 38 grams. The advantage of these projectiles is that they are stable during fluid penetration, and therefore produce a very repeatable hydraulic ram effect.

Entrance and exit panels were constructed of 0.063-inch-thick 7075-T6 aluminum. The 12-inch square panels were clamped to the test tank using a frame that had a 10-inch-square inside dimension. The effective panel size is, therefore, a 10-inch square. Strain gages were applied to the panels at points located 1.5 and 3 inches above center. The projectile trajectory aimpoints were at the panel centers for each shot. The gages were applied to both the inside and outside of the panels. Many gage failures were experienced. The leads to the

NWC TP 6770

gages were not firmly attached to the panels. The leads pulled loose from the gages, particularly during shots with high projectile impact velocities.

Fluid pressure was measured by up to six piezoelectric pressure gages. They were typically located 1 1/2 inches above the expected shot line and about 3 inches apart. The peak pressures obtained ranged from 30,000 psi down to 200 psi. The same gages were used for all of the tests; consequently, the low pressure results are somewhat noisy.

A summary of the shot matrix and overall test results is shown in Table 1. Since the target panels were 7075-T6 aluminum, a very brittle alloy, only two target damage types were obtained. At low velocities, a single perforation was obtained. At higher velocities, cracks originating at the perforation extended to the panel edges.

TABLE 1. Shot Matrix and Results Summary.

Shot no.	Panel	Angle, deg	Velocity, ft/s	Result
234	Entrance	0	1019	- ^a
235			3195	F ^b
236			2050	F
237			2550	F
238	Entrance	45	2045	F
239			980	-
240			1563	F
241	Exit	45	1205	F
242			882	-
243	Exit	0	1208	F
244			893	F
245			766	F

^a Minimal damage.

^b Catastrophic failure.

DETAILED ANALYSIS OF SHOT 239

The hydraulic ram analysis is applied to shot 239, a low velocity oblique entrance shot. The panel suffered minimal damage and the strain gages survived the test. The geometry of the test tank, entrance panel, and the cylinder shot line are shown in Figure 10. The tank's X, Y, Z coordinate system is also shown on the figure.

Five pressure gages were used in the shot. They were placed 1 1/2 inches above the shot line and spaced 3 inches apart. The first gage was 3 inches from the impact point. The five pressure gage records are the noisy traces in Figures 11 through 15. For comparison, calculated pressure curves are plotted on the same figures. The analysis assumes a drag coefficient of 0.82. Rigid surface reflections are assumed for the massive bottom and rear walls of the test tank, and a free-surface reflection is assumed for the top. Wave reflections from the other surfaces are ignored. No other assumptions are required. Comparison of experiment with theory is quite good.

NWCTP 6770

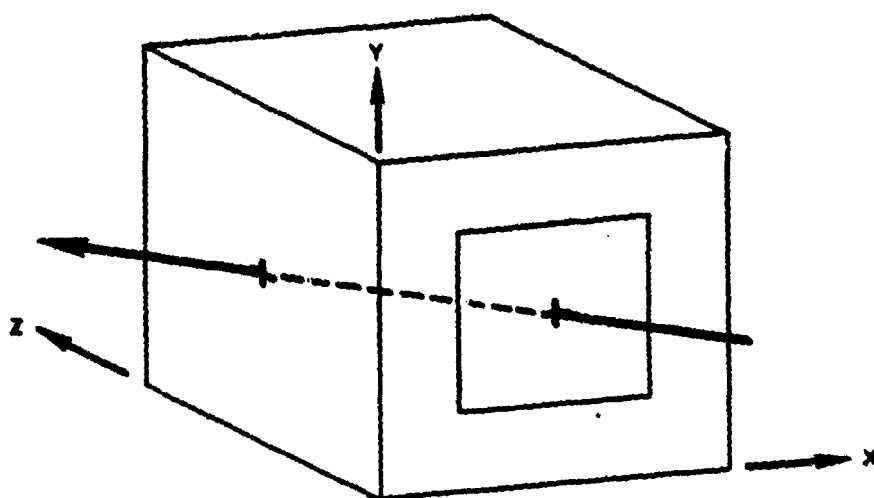


FIGURE 10. Geometry for Shot 239.

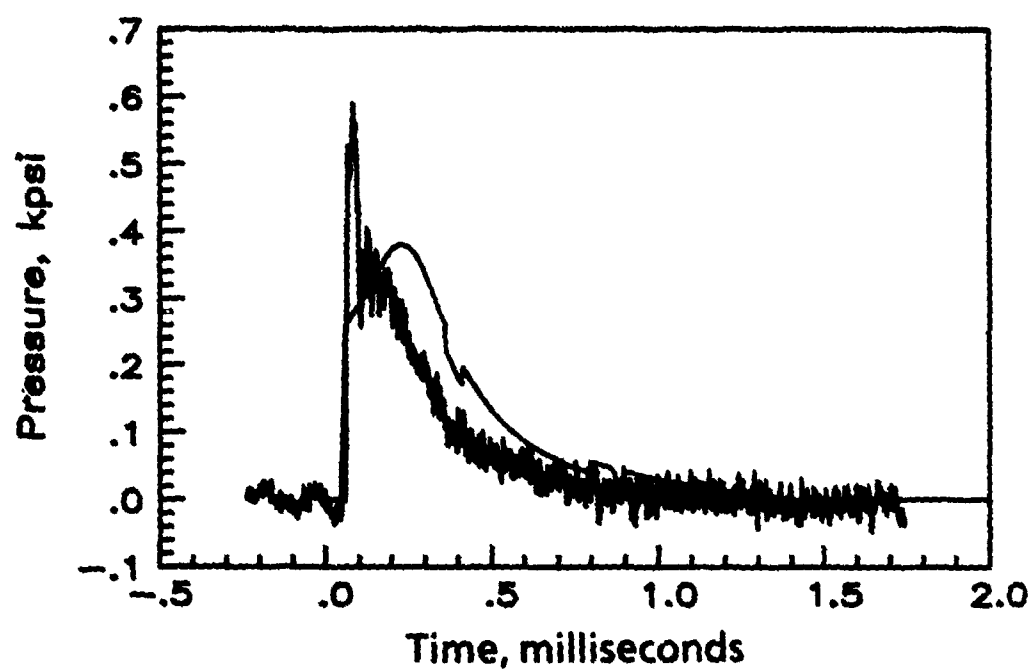


FIGURE 11. Pressure Gage Record No. 1 for Shot 239.

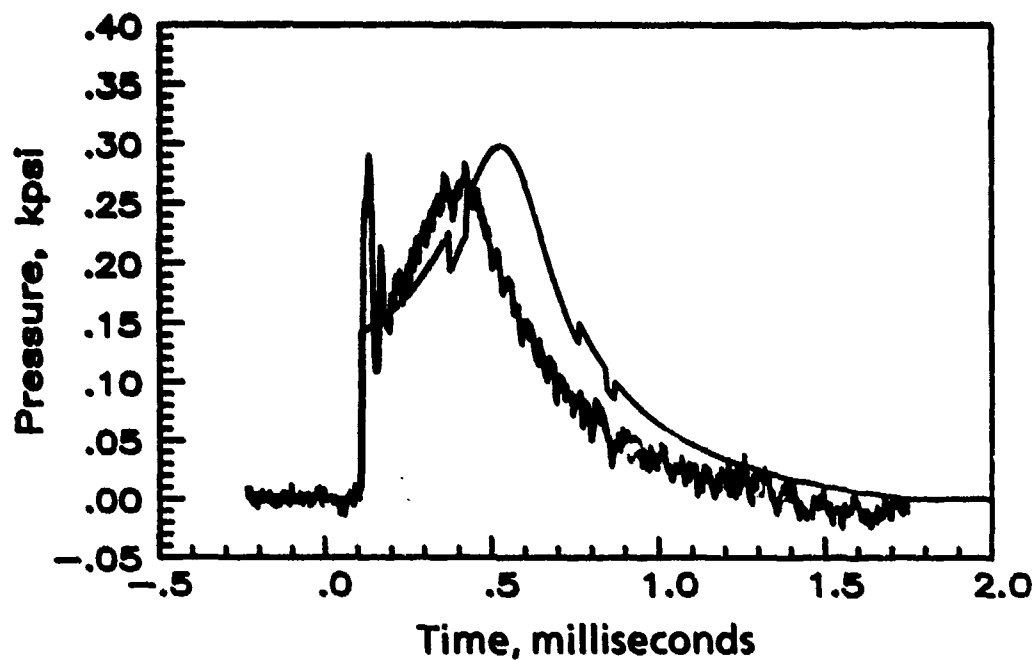


FIGURE 12. Pressure Gage Record No. 2 for Shot 239.

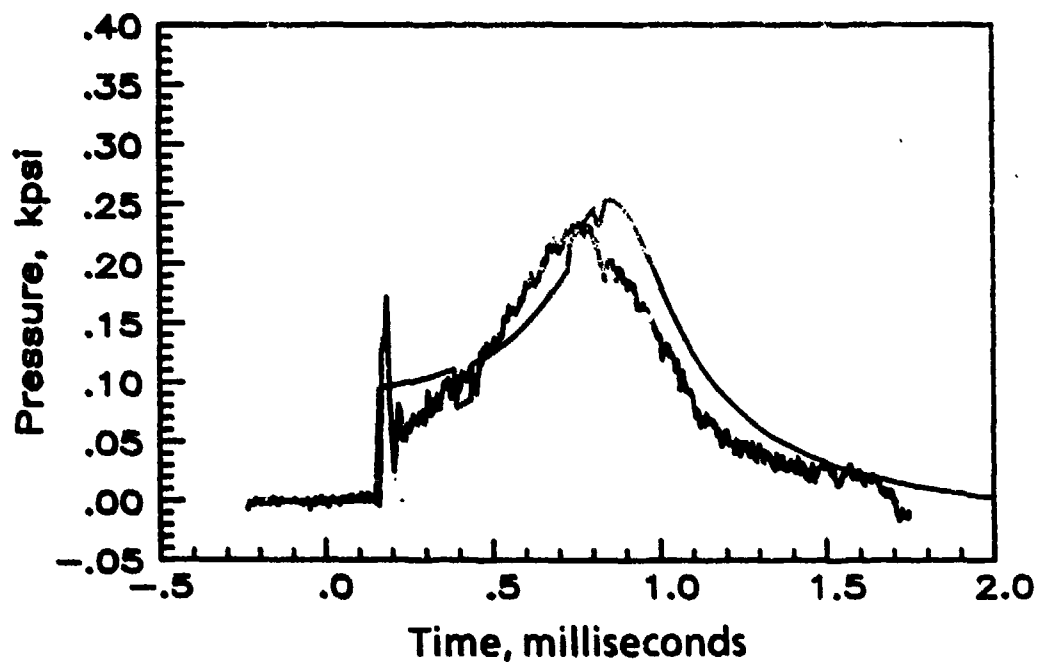


FIGURE 13. Pressure Gage Record No. 3 for Shot 239.

NWCTP 6770

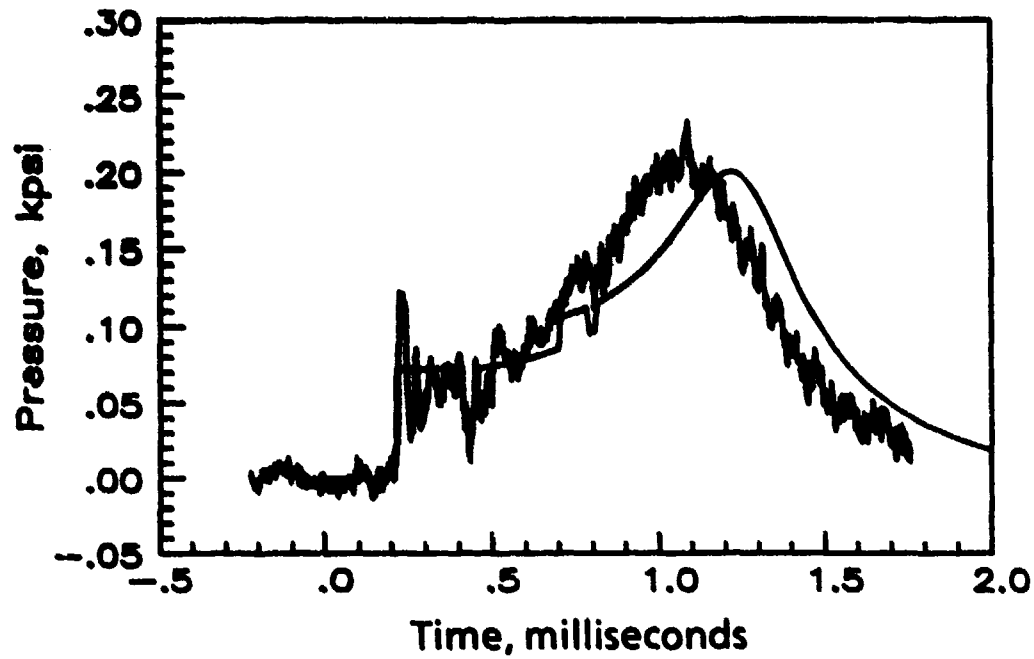


FIGURE 14. Pressure Gage Record No. 4 for Shot 239.

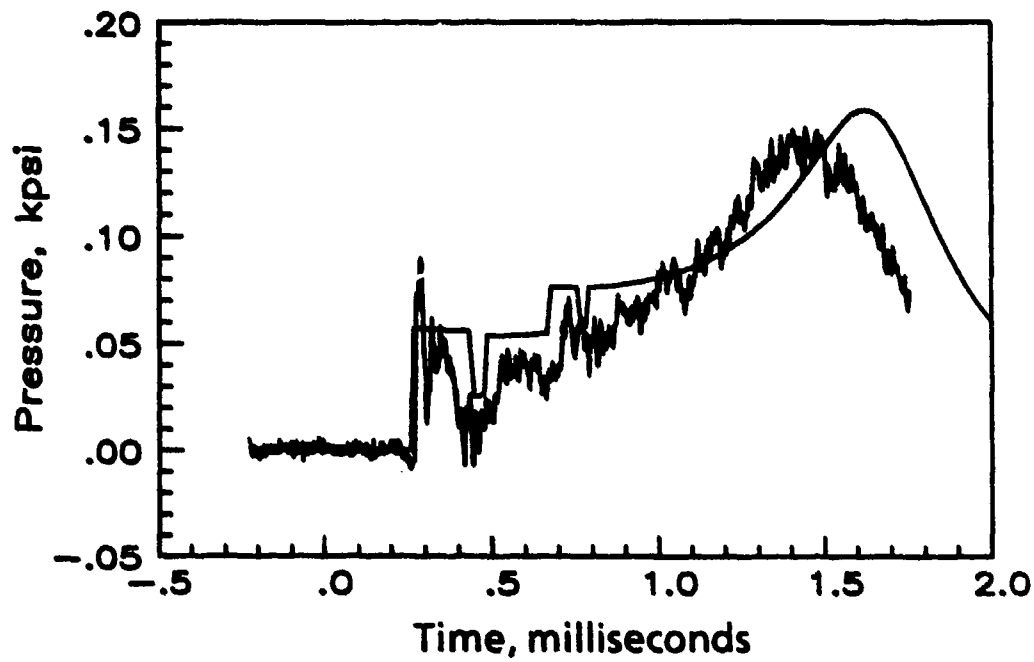


FIGURE 15. Pressure Gage Record No. 5 for Shot 239.

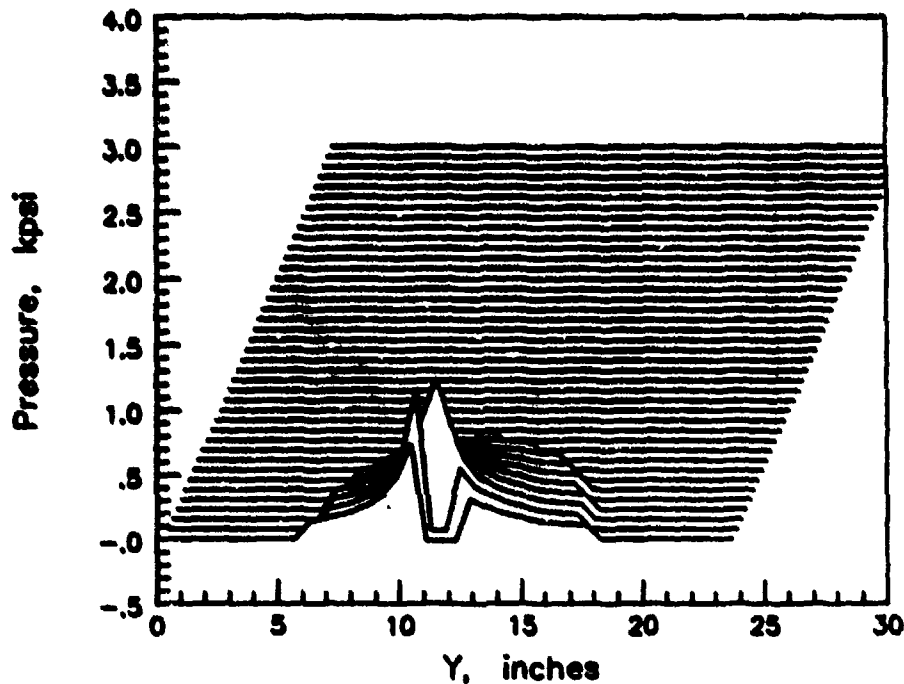


FIGURE 16. Pressure Plot at 0.1 Millisecond After Impact, Shot 239.

Fluid pressure and velocity are calculated over the horizontal plane $Y = \text{constant}$, which contains the shot line (refer to Figure 10). In Figure 16, the pressure is plotted corresponding to a time of 0.1 millisecond after impact. The bottom curve is the pressure on the entrance panel and the top curve is the pressure at the rear wall. In this three-dimensional plot, deflection of a curve in the upward direction indicates a positive pressure at that point. The pressure scale on the left gives the pressure corresponding to a given deflection in a curve. In Figure 16, the highest pressure plotted is about 1.6 kpsi.*

The pressure wave discontinuity arising from impact can be seen propagating away from the point of impact. The fluid cavity behind the projectile can be seen plotted as a region of zero absolute pressure. The pressure is highest in the vicinity of the projectile. Figures 17 and 18 show the pressure distribution at 0.5 and 1.3 milliseconds, respectively, after impact. The region of high pressure moves with the projectile, and the cavity increases in size. After the projectile exits the tank, the pressure drops to a comparatively low level. In Figures 16-18 the pressure wave reflections were not calculated.

Fluid velocity at 0.1 and 1.0 millisecond after impact is plotted in Figures 19 and 20. The quantity actually plotted is ρcu where ρ is fluid density, c is fluid sound speed, and u is fluid velocity. The product has the dimensions of pressure. It enters into the variable image

* kpsi means thousand pounds per square inch.

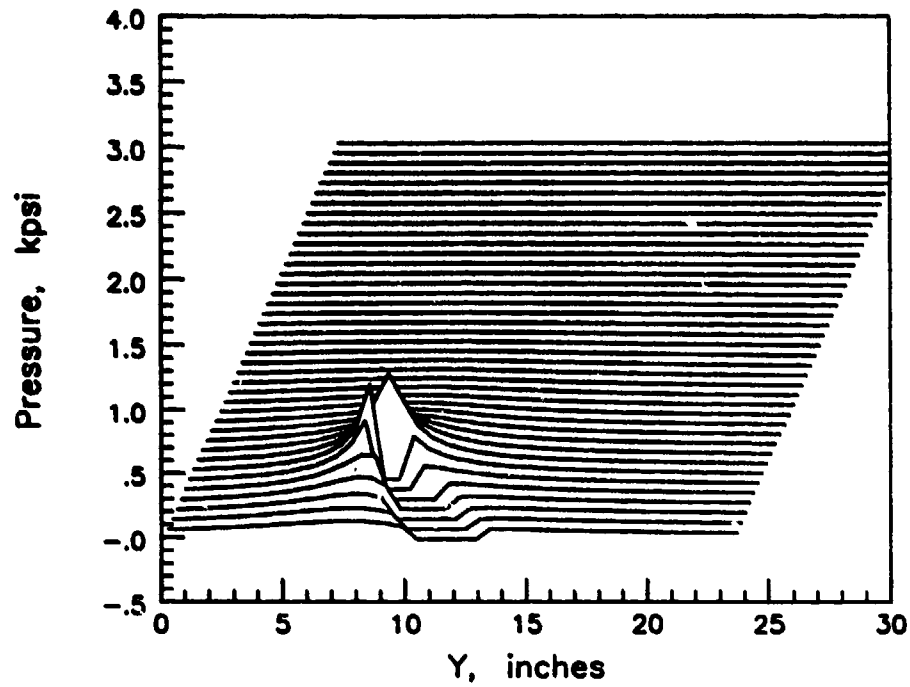


FIGURE 17. Pressure Plot at 0.5 Millisecond After Impact, Shot 239.

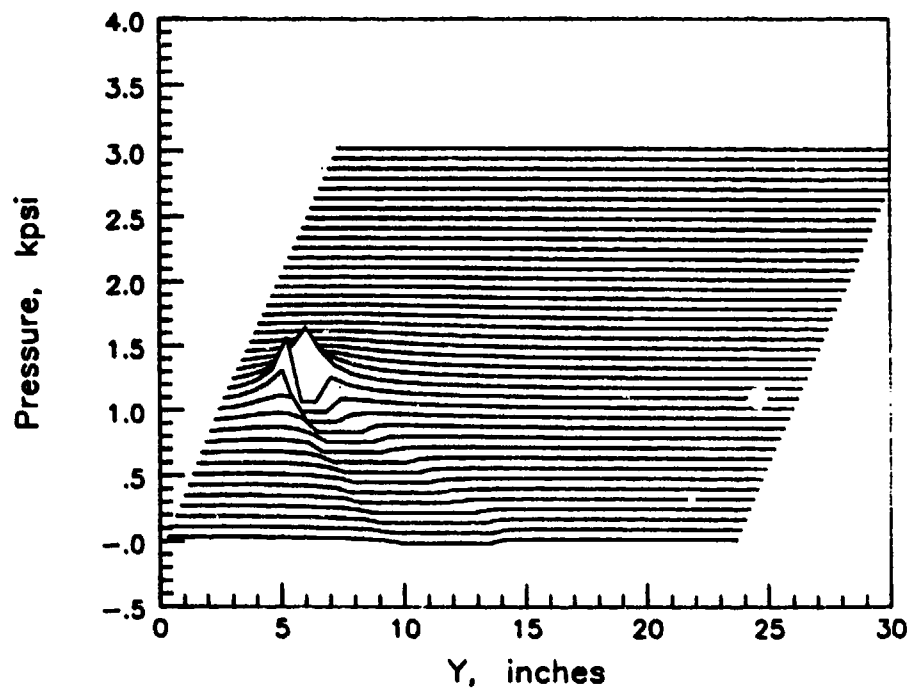


FIGURE 18. Pressure Plot at 1.3 Milliseconds After Impact, Shot 239.

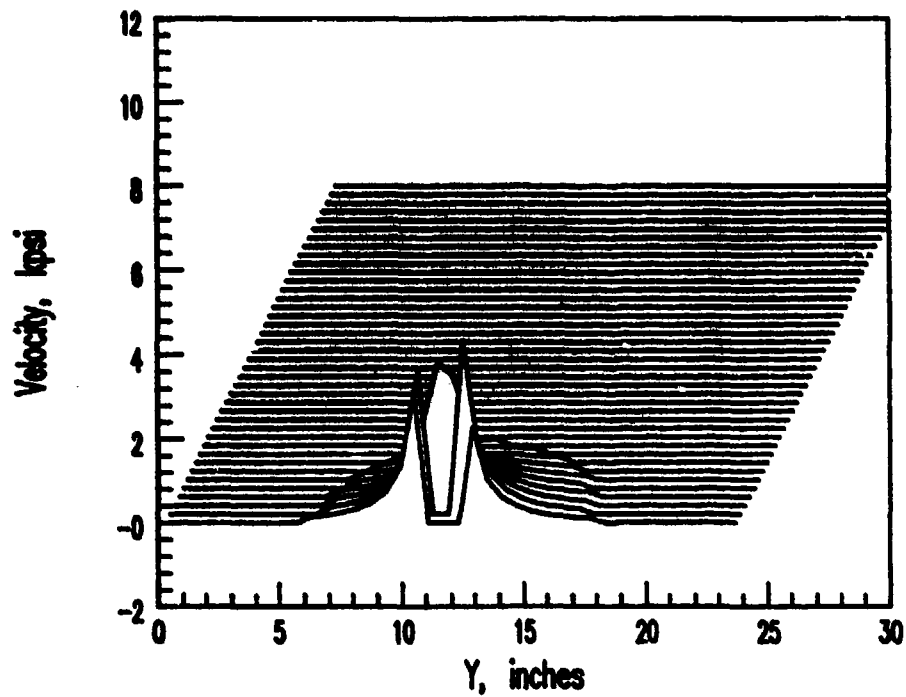


FIGURE 19. Fluid Velocity at 0.1 Millisecond After Impact, Shot 239.

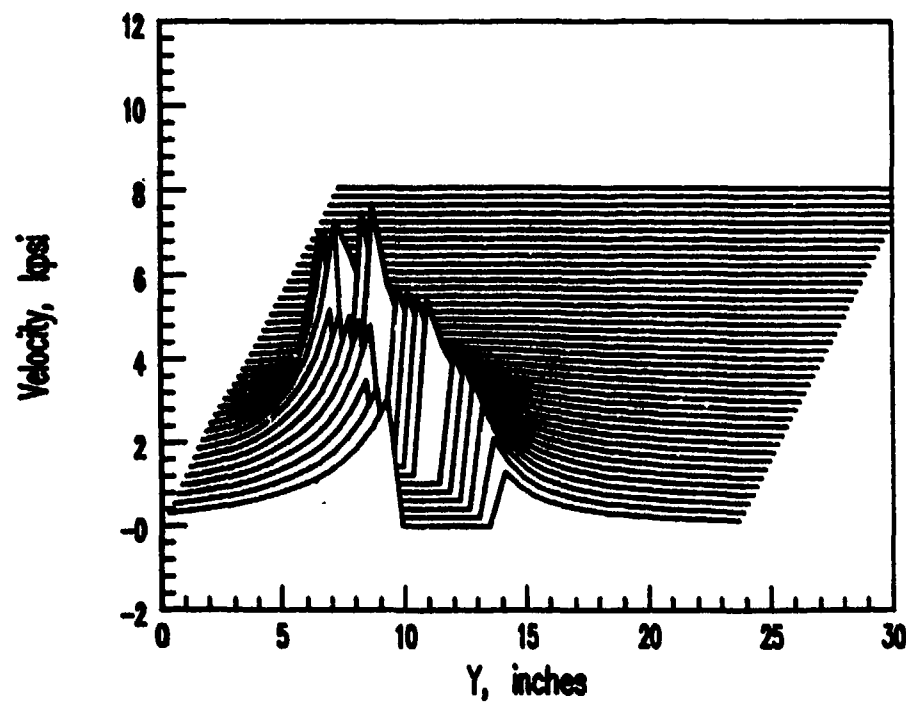


FIGURE 20. Fluid Velocity at 1.0 Millisecond After Impact, Shot 239.

(Equation 31) in the same role as pressure. The velocity plots have two differences from the pressure plots: the peak velocity is found on the cavity surface, not just near the projectile, and the high fluid velocity remains even after the projectile exits the fluid. The magnitude of the peak velocity, pcu , is about three times the pressure peak. According to Equation 31, the fluid velocity is going to play an important role in the wall pressure loading.

Structural reaction of the entrance panel was calculated using the assumption of a Gaussian panel deflection. The resulting peak deflection is plotted in Figure 21. It rises monotonically to 0.7 inch during the 5.0-millisecond period analyzed. The motion of the center of the Gaussian deflection is plotted in Figure 22. Both the x and y coordinates are initially at 5 inches, the impact point at the center of the 10-inch square panel. The x coordinate follows the motion of the projectile until, after about 2 milliseconds, it lies outside of the entrance panel. Because of the symmetry of the panel pressure loading, the y coordinate of the Gaussian center is not expected to move, and it does not.

The widths of the Gaussian profile in the x and y directions are plotted in Figure 23. They both grow rapidly until at 1 millisecond they exceed the panel boundaries. It is important to remember that the Gaussian deflection structural model represents an infinite plate that is loaded only in the area of the actual panel.

In the Lagrangian formulation of structural response, the wall loading is expressed by generalized forces defined by Equation 42. Therefore, the most appropriate measure of wall

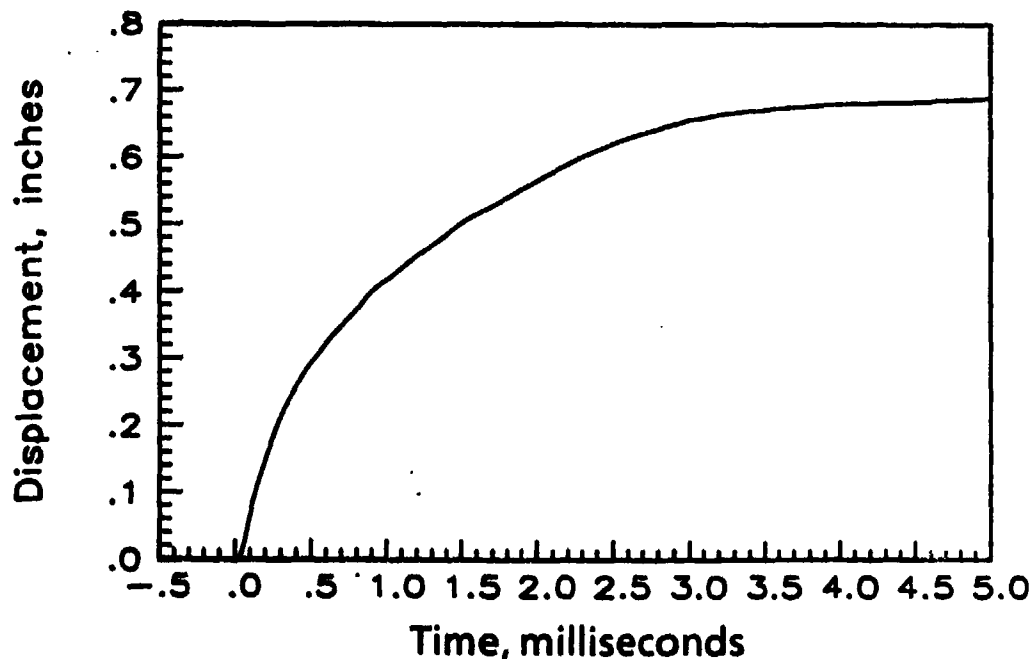


FIGURE 21. Gaussian Panel Deflection Showing Resulting Peak Deflection.

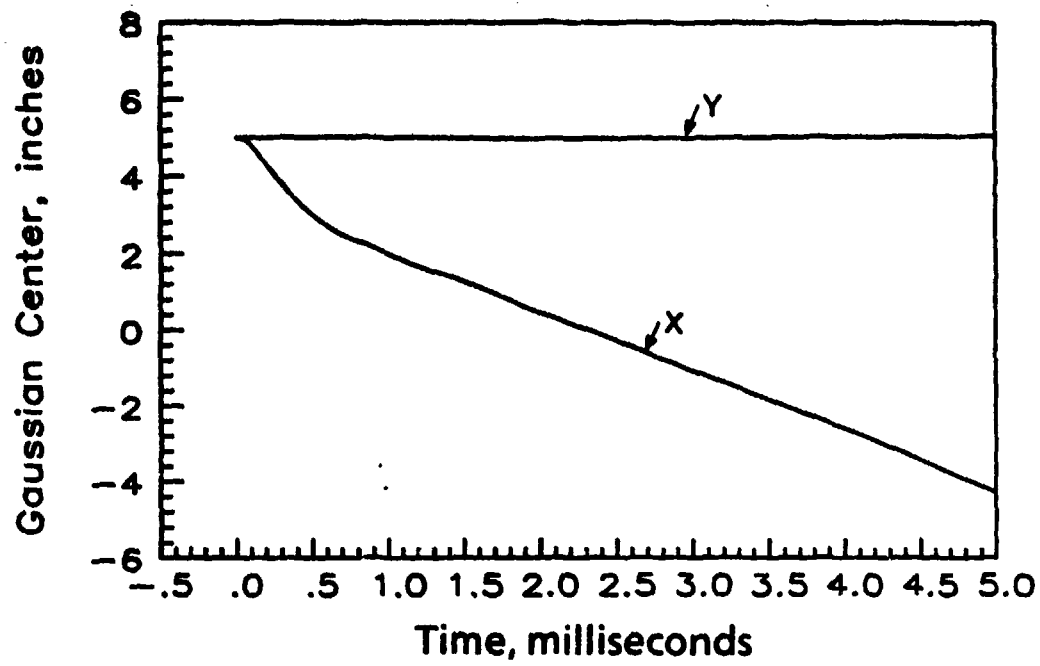


FIGURE 22. Motion of Center of Gaussian Panel Deflection.

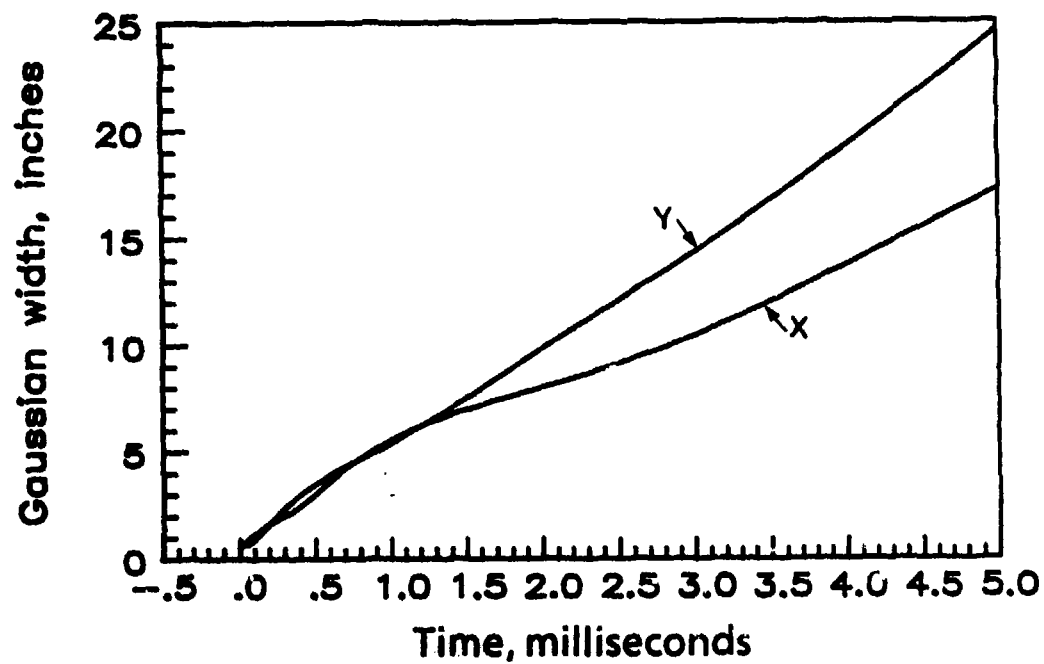


FIGURE 23. Widths of Gaussian Profile in x and y Directions.

loading is a weighted average over the surface of the wall. For any quantity, f , the weighted average, \bar{f} , is defined as

$$\bar{f} = \frac{1}{N} \iint f w \, dx dy$$

where

$$N = \iint w \, dx dy$$

The integrals are taken over the wall surface and the w are the wall normal displacement functions.

Weighted averages of the incident pressure and normal fluid velocity are plotted in Figure 24 as a function of time. For velocity, the quantity $\rho c u$, which has the dimensions of pressure, is plotted. In Reference 8, the "piston" theory of the fluid/structure interaction was shown to give poor correlation of theory and experiment. The piston theory is appropriate when $P = \rho c u$ which, according to Figure 24, is not valid. After an initial transient, it is apparent that the fluid velocity provides the dominant wall loading mechanism.

The weighted average of the total wall pressure loading is shown in Figure 25. The magnitude of the wall pressure is low compared to the incident pressure and fluid velocity because motion of the wall causes pressure relief at the wall. The jagged appearance of the

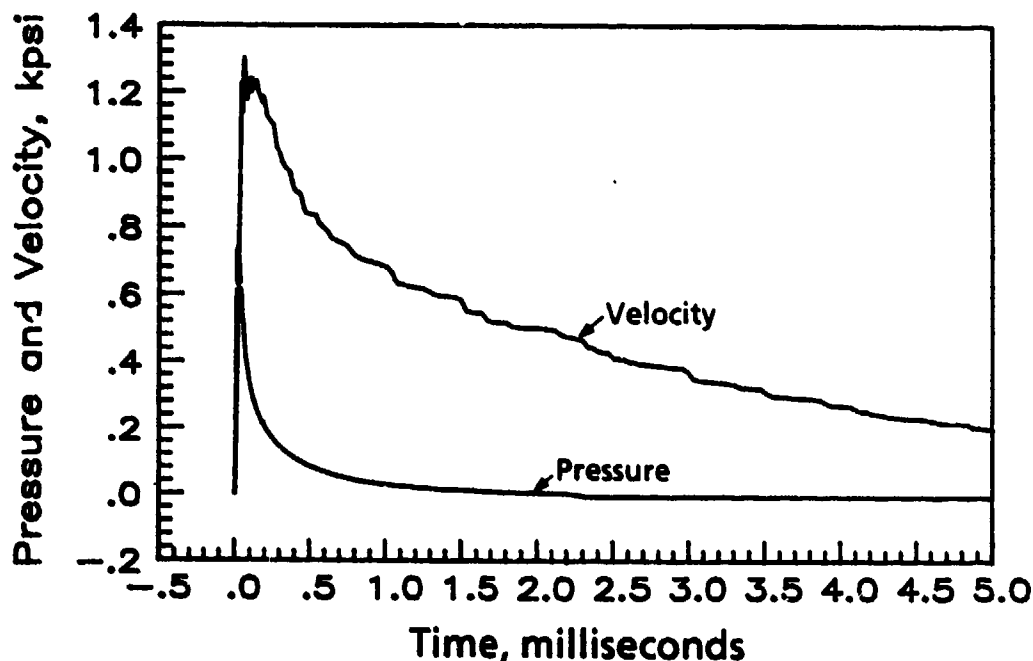


FIGURE 24. Weighted Averages of Incident Pressure and Normal Fluid Velocity.

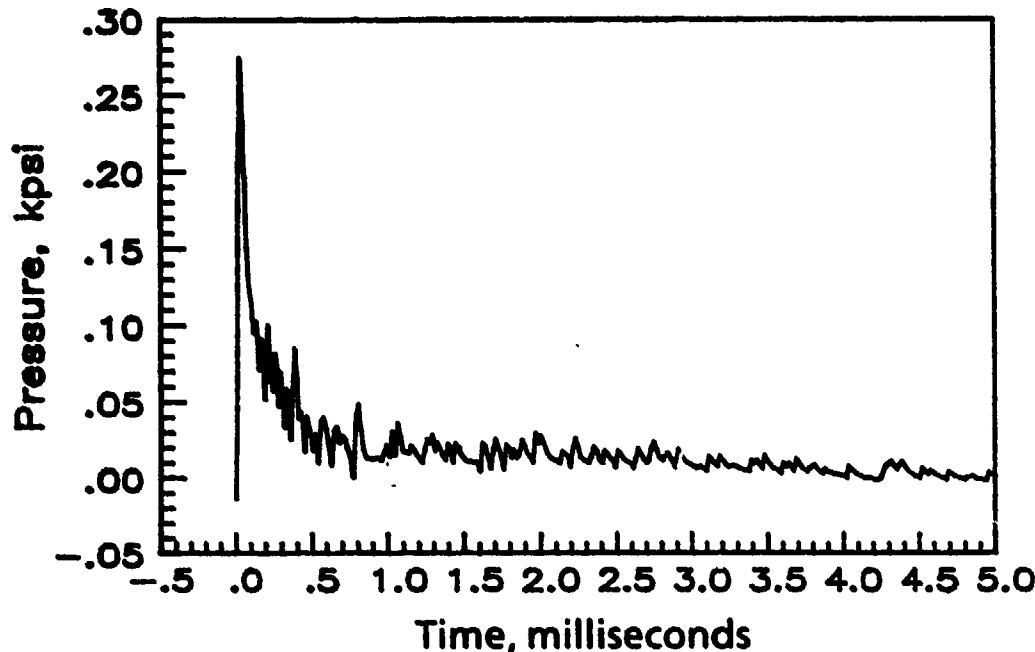


FIGURE 25. Weighted Average of Total Wall Pressure Loading.

pressure curve is caused by cavitation collapse at the wall surface. The collapse process actually produces a continuous pressure, but subdivision of the wall into numerous computational elements separates the collapse pressure into a series of pressure pulses.

The growth and collapse of cavitation at the wall is shown in Figure 26. The curve labeled pressure is the fraction of the wall surface area that is covered with cavitation and the constant pressure boundary condition is satisfied. The curved labeled velocity is the fraction of the wall surface area wetted by the fluid and where the fluid velocity must equal the wall velocity. The fluid curve, labeled central cavity, is the area fraction of the cavity following behind the projectile. Initially, the entire panel is wetted. The intense pressure loading at the penetration site pushes the wall away from the fluid over the remainder of the panel until at about 0.5 millisecond the wall is almost entirely cavitated. Thereafter, the fluid catches up to the wall and the region of cavitation shrinks.

When using Gaussian deflection profiles, wall cavitation will be exaggerated whenever the width of the Gaussian is commensurate with the width of the wall. This results from ignoring the clamped boundary condition at the panel edges.

The area fraction of the panel covered by the central cavity is significant. At 5.0 milliseconds, Figure 26 shows that the central cavity has grown to cover 40% of the entire entry wall.

The average value of the variable image theory Q function is plotted in Figure 27. The initial value is $Q = 1$. The wall initially reflects pressure waves like a rigid wall. When the wall moves outward in response to the initial pressure, the Q drops very rapidly. When

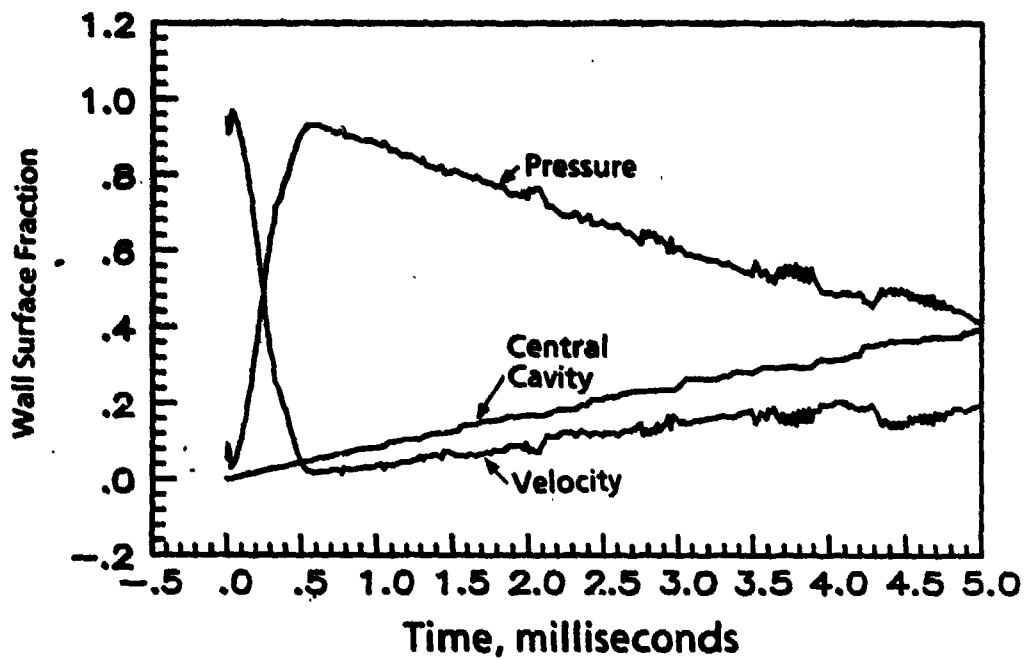


FIGURE 26. Growth and Collapse of Cavitation at Wall.

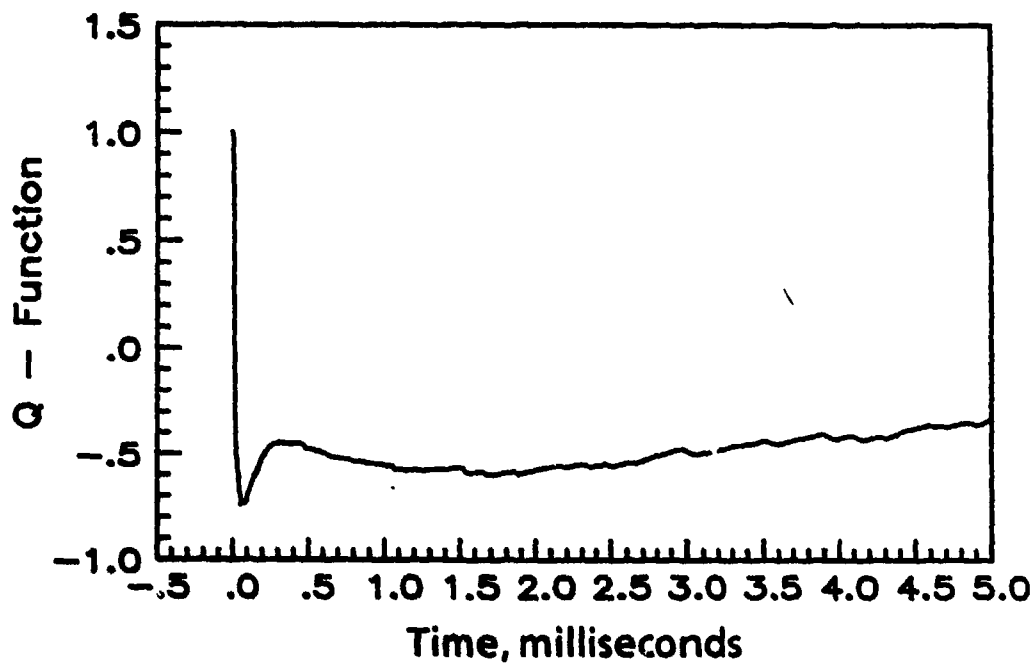


FIGURE 27. Average Value of Variable Image Theory Q Function.

$Q = -1$, the wall surface reflects pressure waves like a free surface. The value of Q seems to stabilize at about $Q = -0.5$, which may be an artifact of the averaging for this particular problem.

The peak wall membrane stresses calculated at the Gaussian center are shown in Figure 28. The peak stress is larger in the X direction, which results from a smaller Gaussian width in this direction. The maximum stress is about 45 kpsi, which is significantly less than the yield stress of 73 kpsi for the material. The panel did not fail, but it had a barely noticeable permanent deformation near the impact perforation. This deformation would have resulted from additional bending stresses not shown in Figure 28. Wall strain energy is shown in Figure 29. Most of the energy is in the form of membrane stresses, particularly at later times. The wall mass is so low that the kinetic energy is never significant.

Geometry of the entrance panel for shot 239 showing strain gage locations is shown in Figure 30. Table 2 gives the data for each gage.

The experimental strain gage data are shown compared to corresponding calculated strains in Figures 31 through 36. It is obvious from the figures that the simple Gaussian structural deflection is not suitable to predict the details of the strain records. In fact, some of the grosser features, such as the large compression obtained experimentally for the Y strains on the wet side gages, were not predicted by theory. The Gaussian deflection profile predictions are, however, much better than similar predictions using the cosine deflection profiles for impact walls.

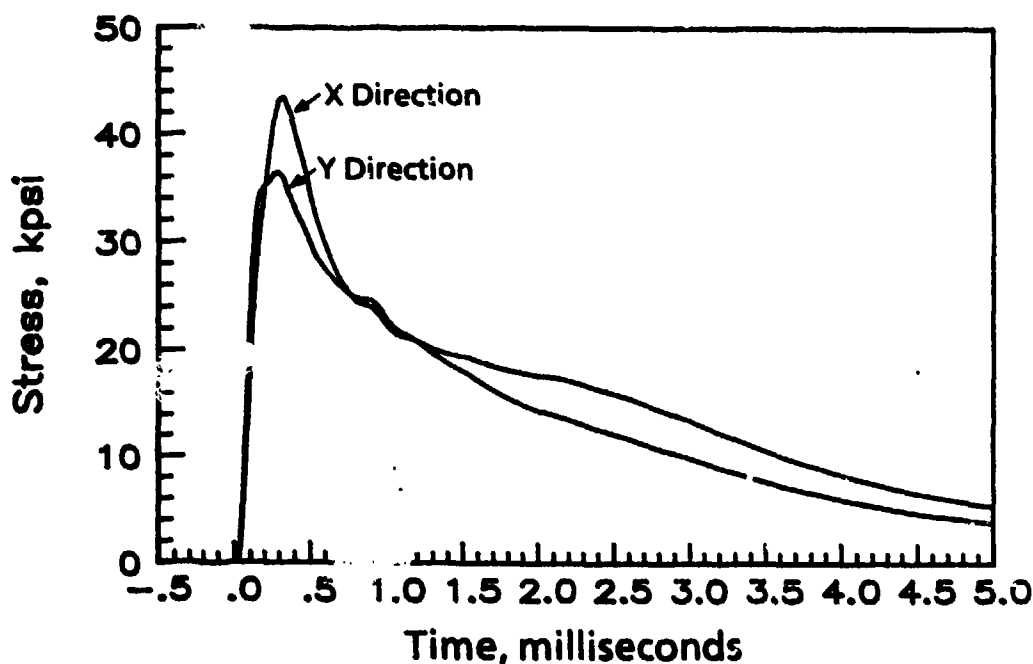


FIGURE 28. Peak Wall Membrane Stresses Calculated at Gaussian Center.

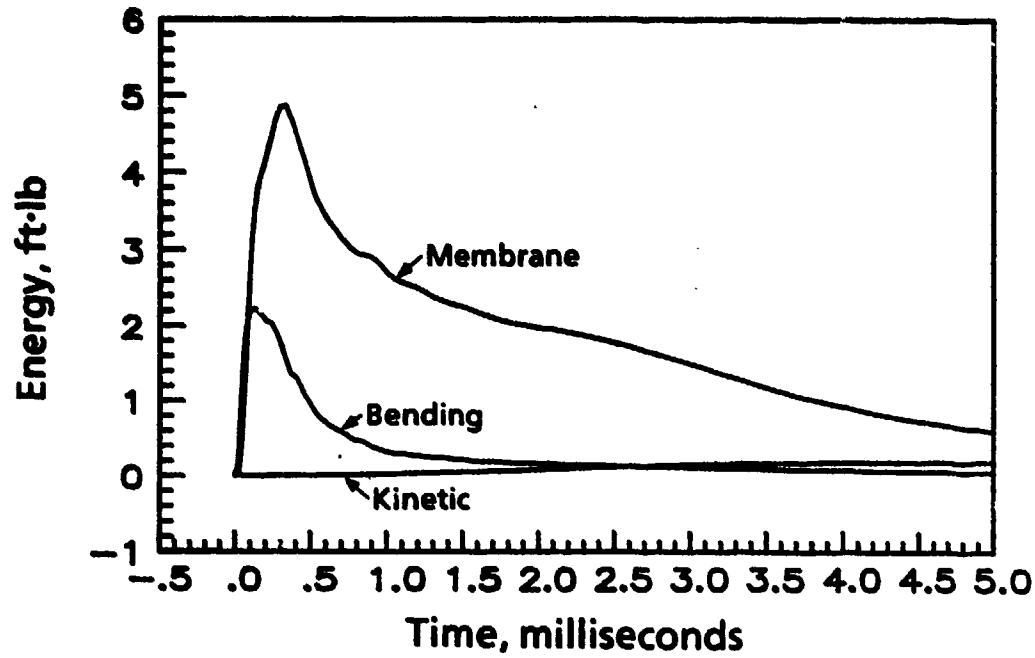


FIGURE 29. Wall Strain Energy.

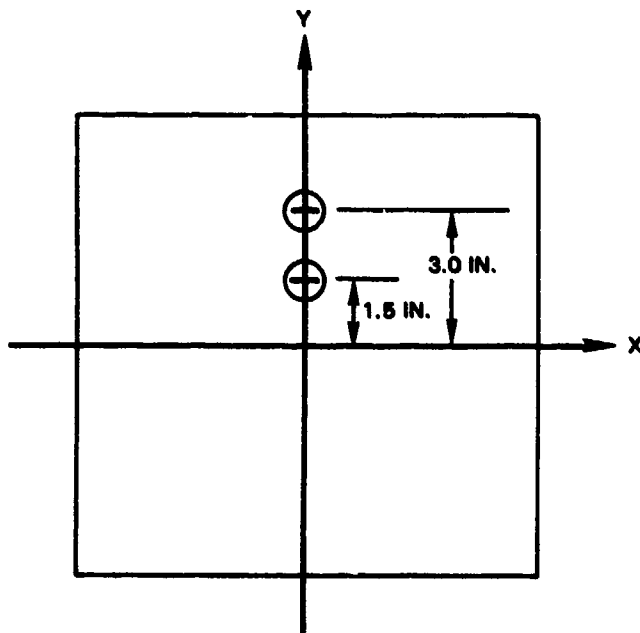


FIGURE 30. Entrance Panel Geometry Showing Location of Strain Gages for Shot 239.

TABLE 2. Strain Gage Location and Orientation for Shot 239.

Gage no.	Y offset, in.	Strain direction	Side
1	3	Y	Wet
2	3	X	Wet
3	1.5	Y	Wet
4	1.5	X	Wet
5	3	Y	Dry
6	3	X	Dry

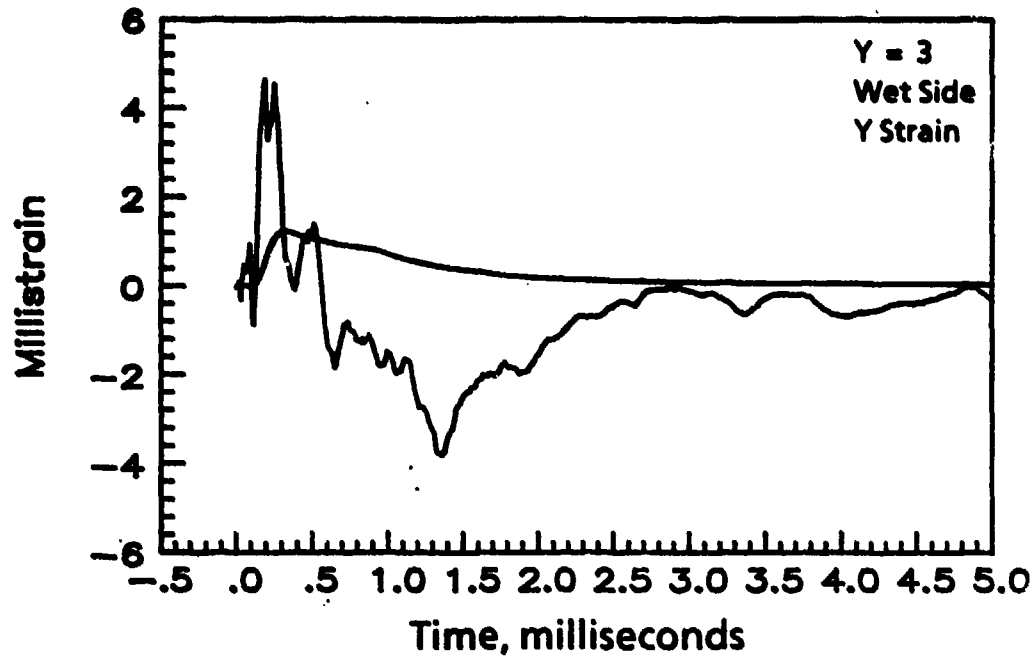


FIGURE 31. Experimental Strain Gage Data Compared to Corresponding Calculated Strains, No. 239-1.

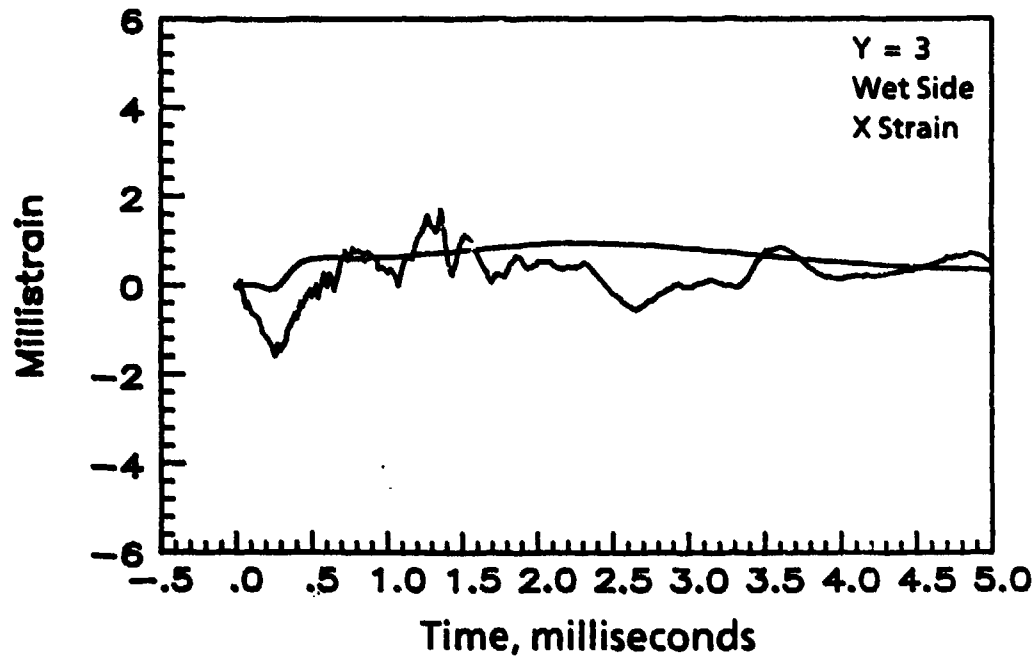


FIGURE 32. Experimental Strain Gage Data Compared to Corresponding Calculated Strains, No. 239-2.

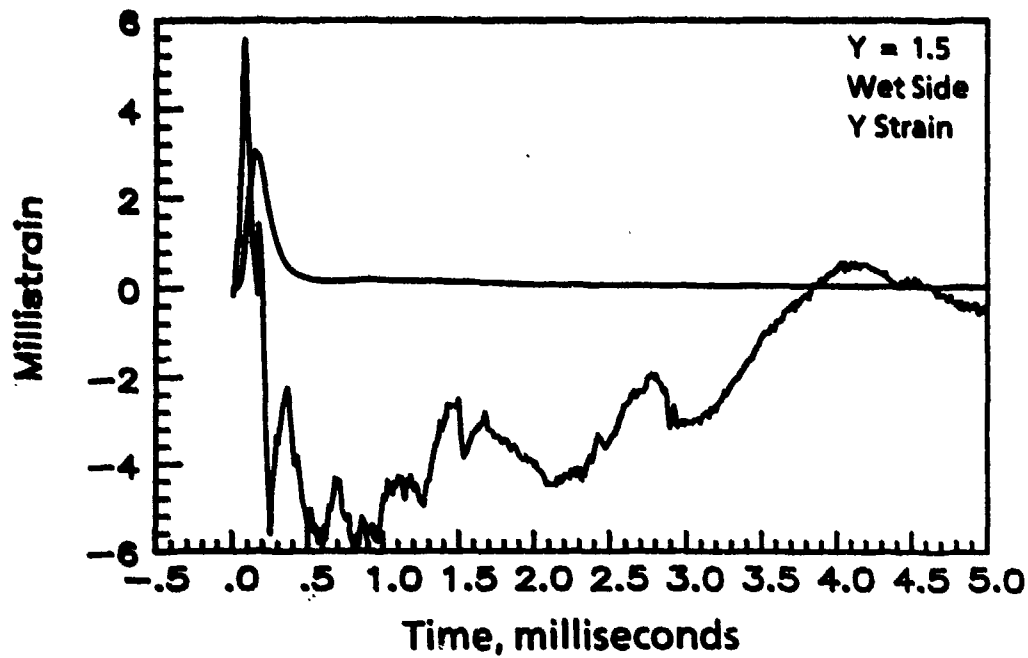


FIGURE 33. Experimental Strain Gage Data Compared to Corresponding Calculated Strains, No. 239-3.

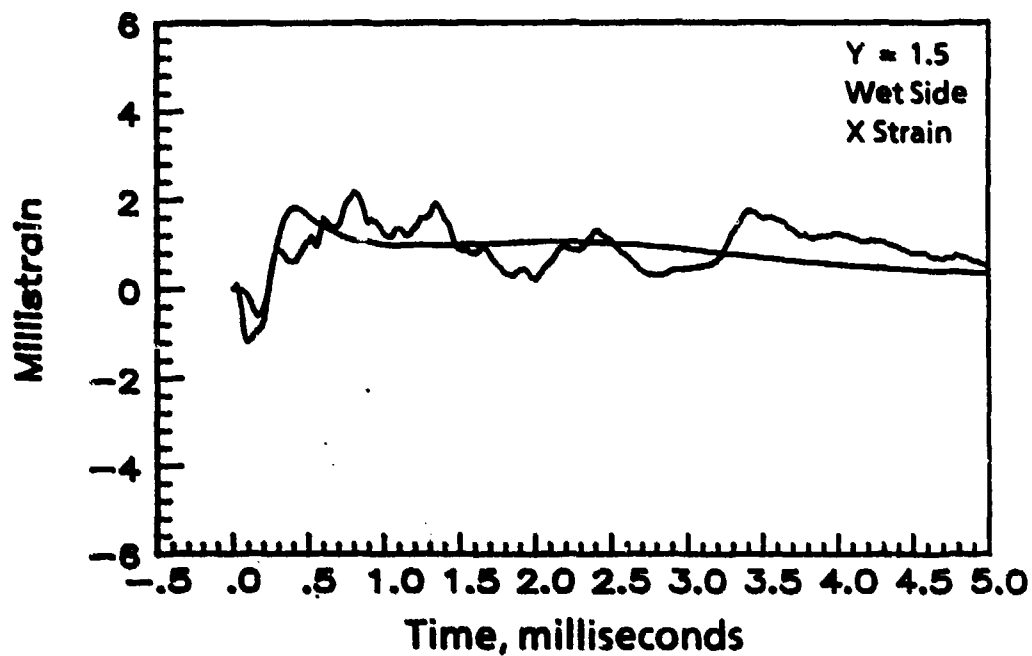


FIGURE 34. Experimental Strain Gage Data Compared to Corresponding Calculated Strains, No. 239-4.

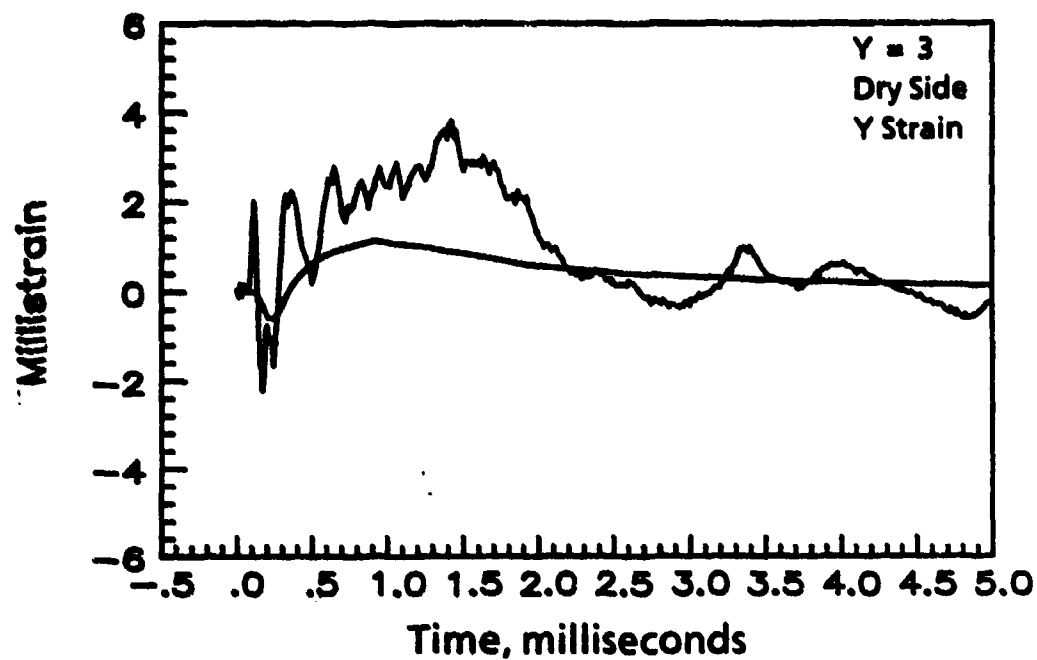


FIGURE 35. Experimental Strain Gage Data Compared to Corresponding Calculated Strains, No. 239-5.

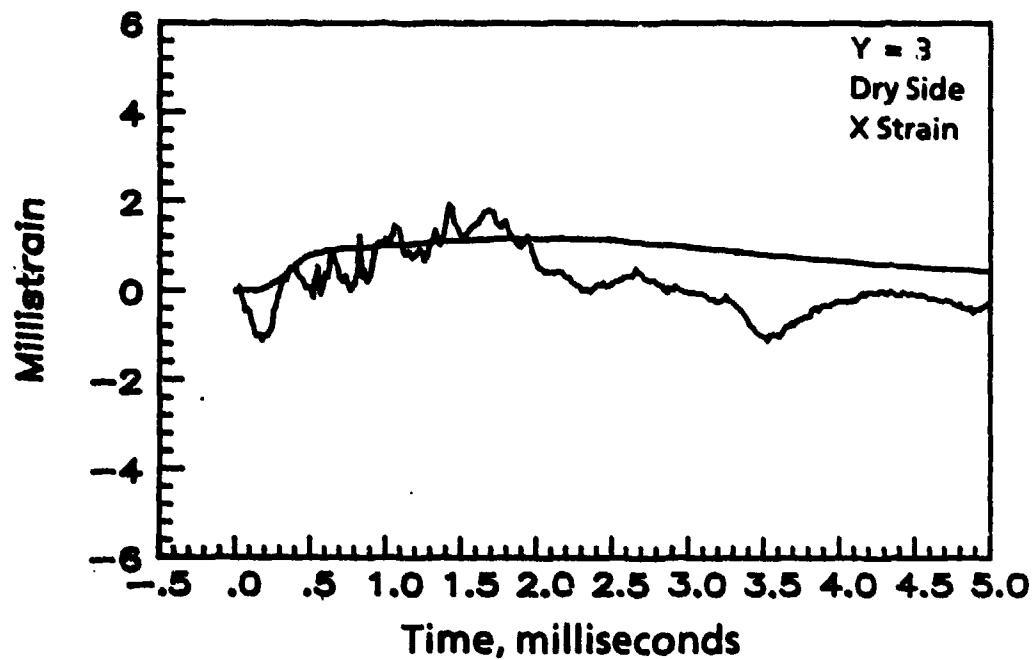


FIGURE 36. Experimental Strain Gage Data Compared to Corresponding Calculated Strains, No. 239-6.

The agreement between experiment and theory is the best that has been obtained to date with the simple structural theories. A more refined calculation using a finite element model would explain the discrepancies obtained in this report.

In order to understand the hydraulic ram phenomena, the spacial, as well as temporal, variation of the fluid and wall panel properties over the surface of the wall are of interest. Plots showing spacial distribution are shown at incident pressure (Figure 37), incident normal velocity (Figure 38), total wall pressure (Figure 39), panel deflection (Figure 40), wall cavitation (Figure 41), and the variable image Q function (Figure 42).

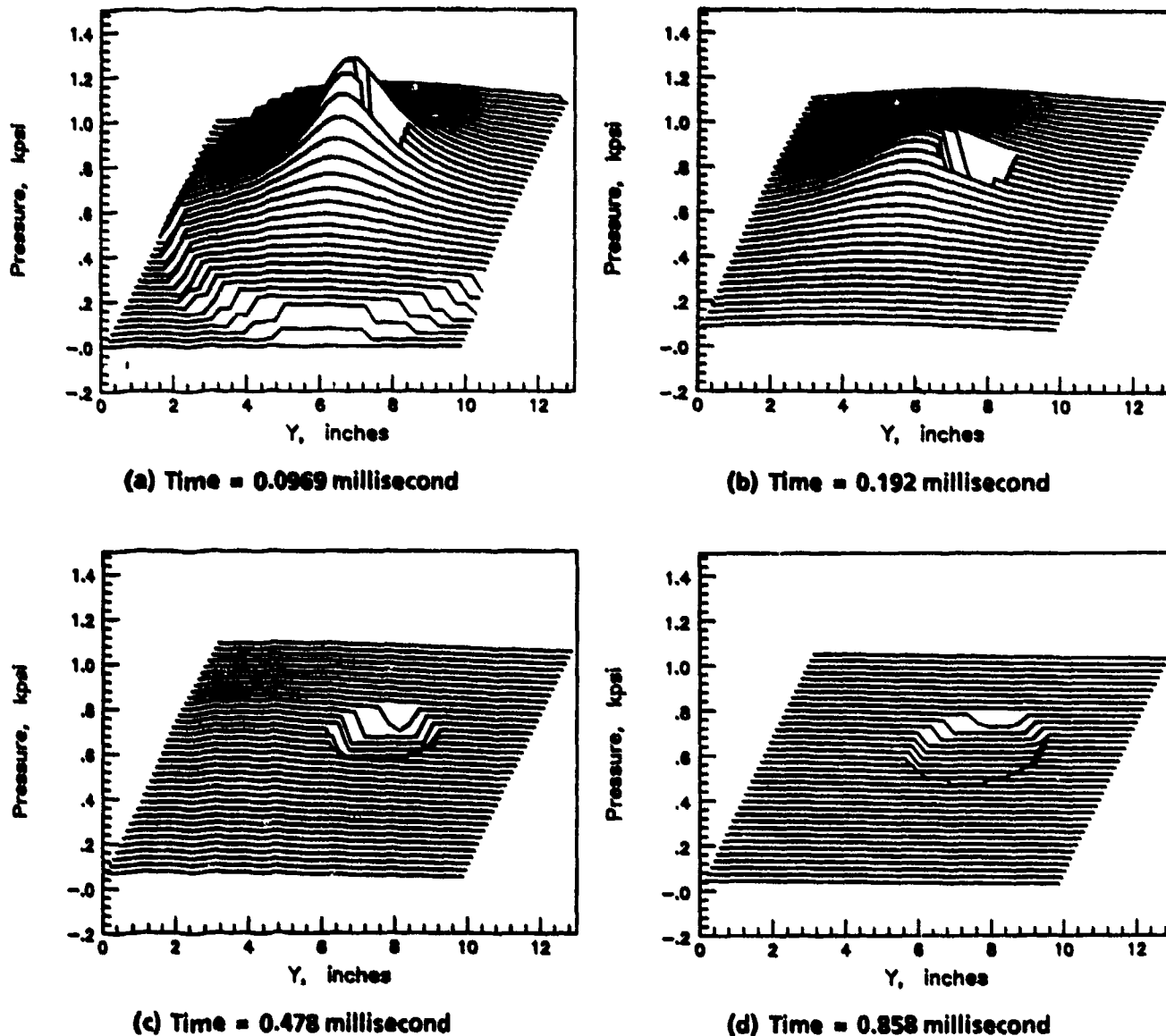
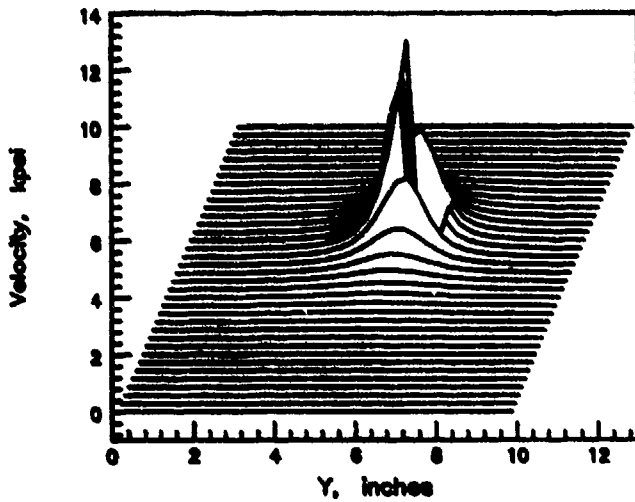
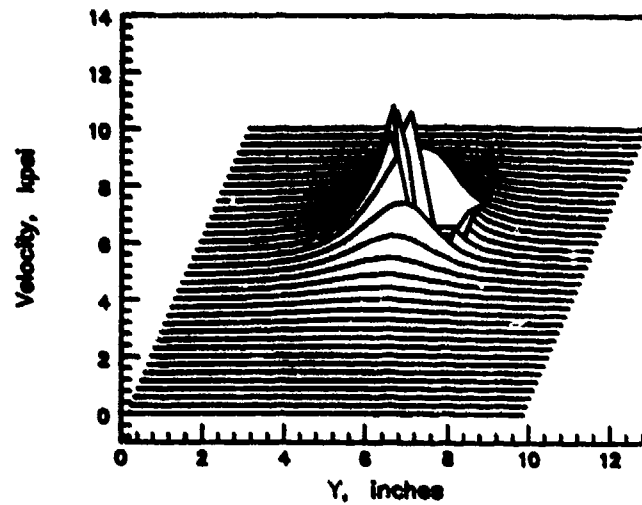


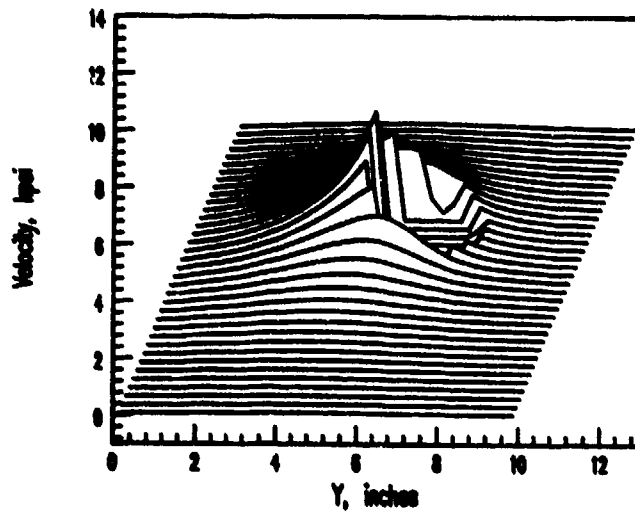
FIGURE 37. Spatial Distribution of the Incident Pressure.



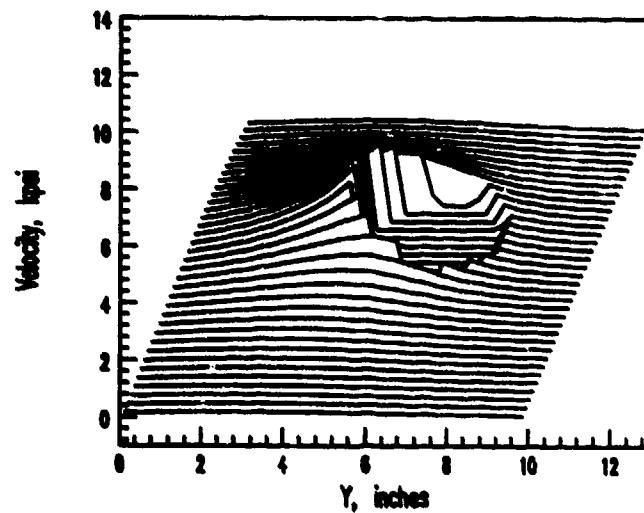
(a) Time = 0.0969 millisecond



(b) Time = 0.192 millisecond

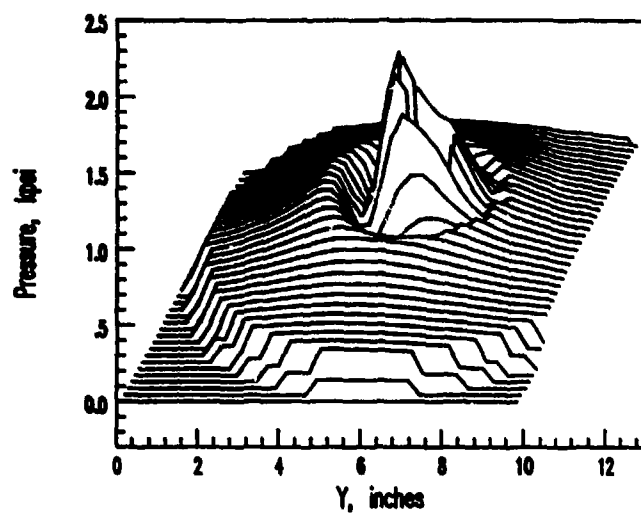


(c) Time = 0.478 millisecond

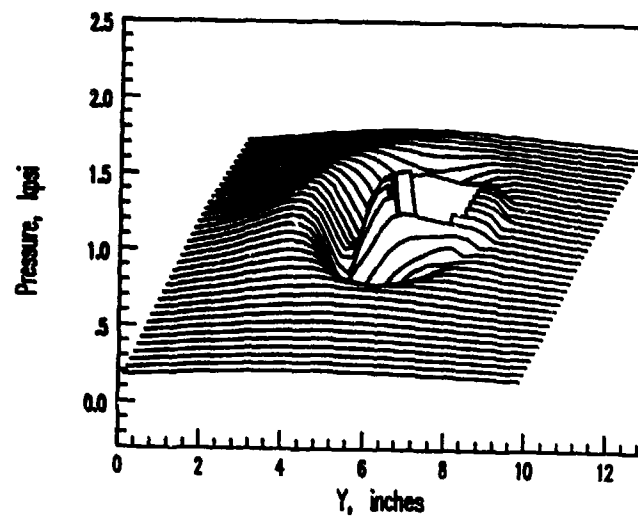


(d) Time = 0.858 millisecond

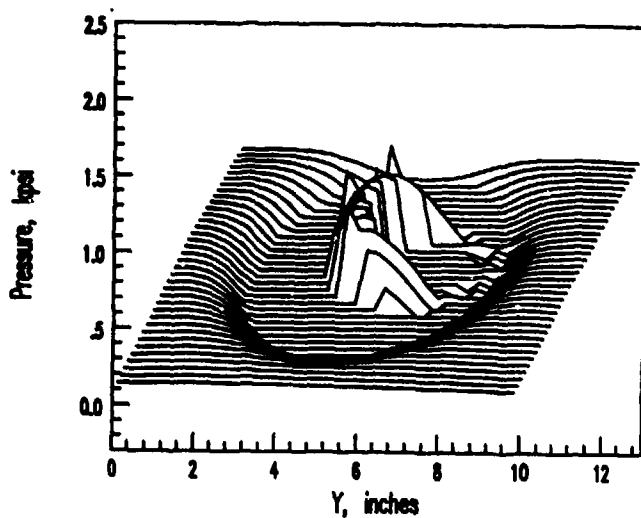
FIGURE 38. Spatial Distribution of the Incident Normal Velocity.



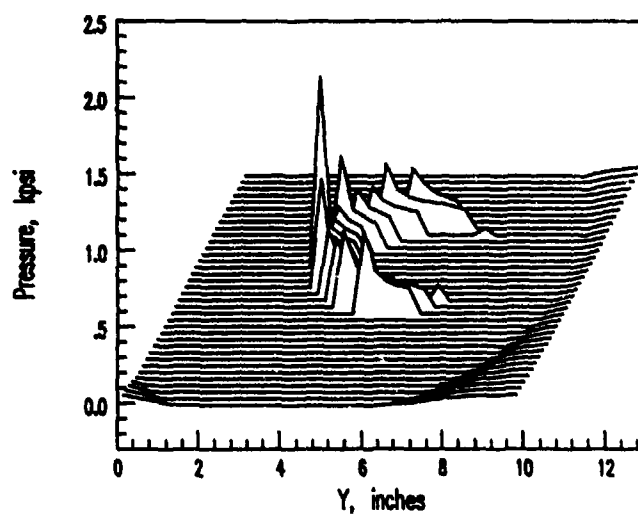
(a) Time = 0.0969 millisecond



(b) Time = 0.192 millisecond

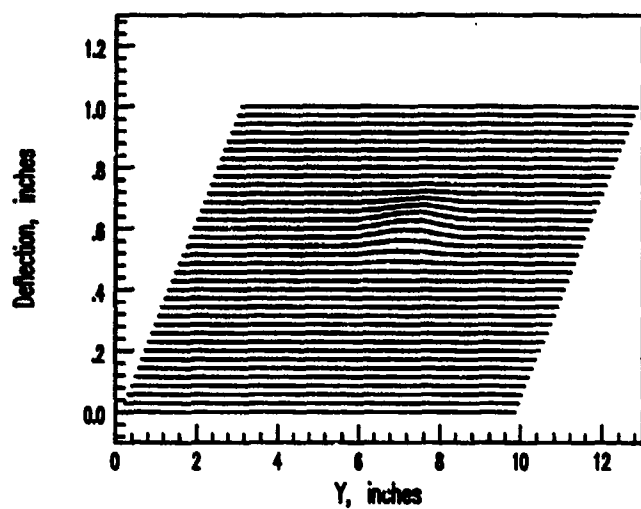


(c) Time = 0.478 millisecond

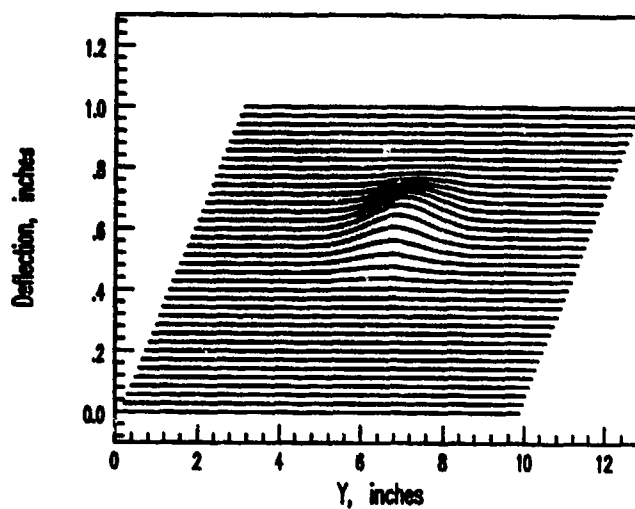


(d) Time = 0.858 millisecond

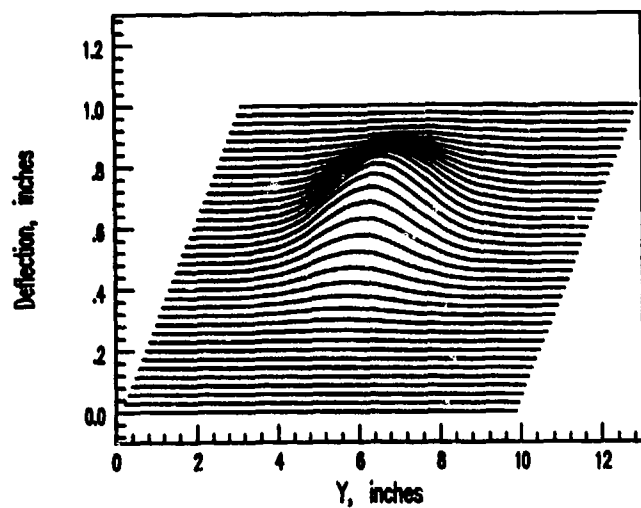
FIGURE 39. Spatial Distribution of the Total Wall Pressure.



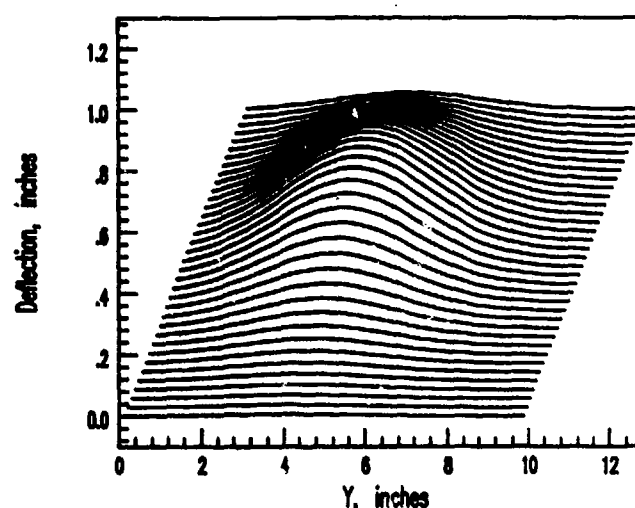
(a) Time = 0.0969 millisecond



(b) Time = 0.192 millisecond

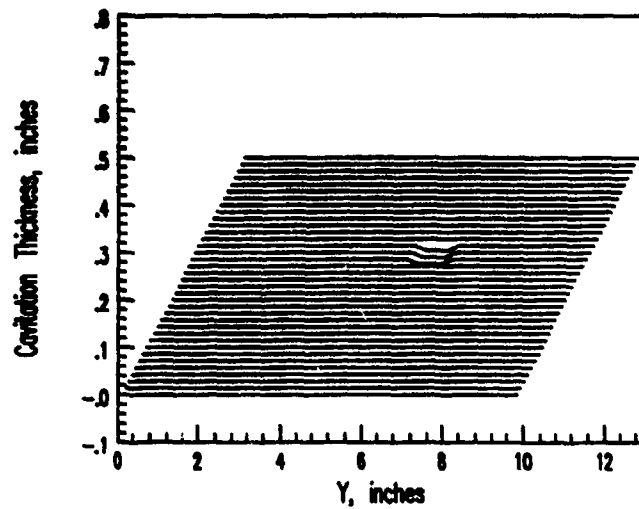


(c) Time = 0.478 millisecond

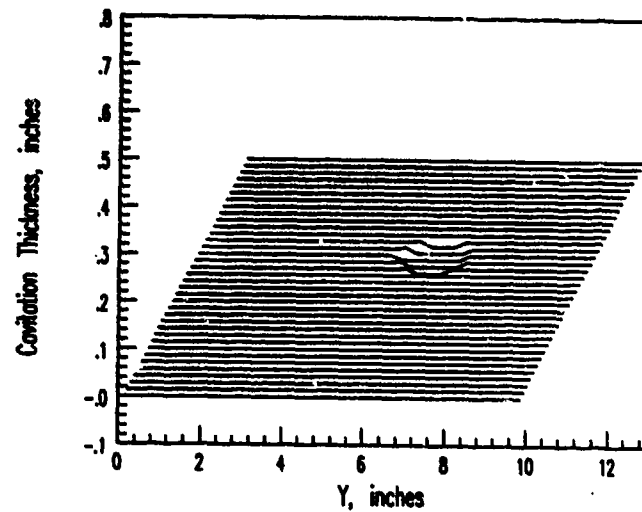


(d) Time = 0.858 millisecond

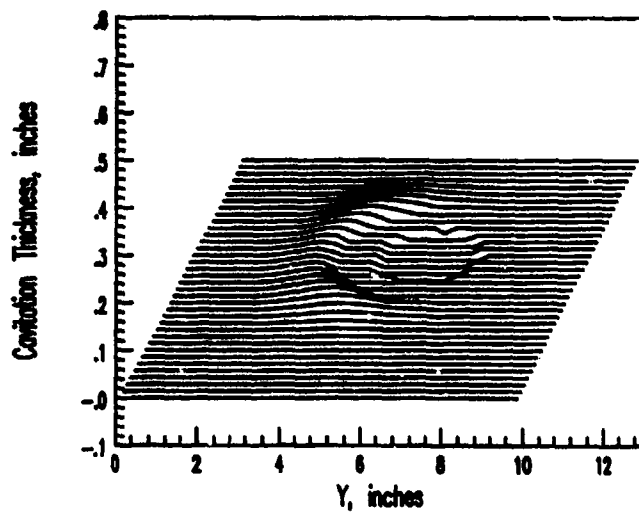
FIGURE 40. Spatial Distribution of the Panel Deflection.



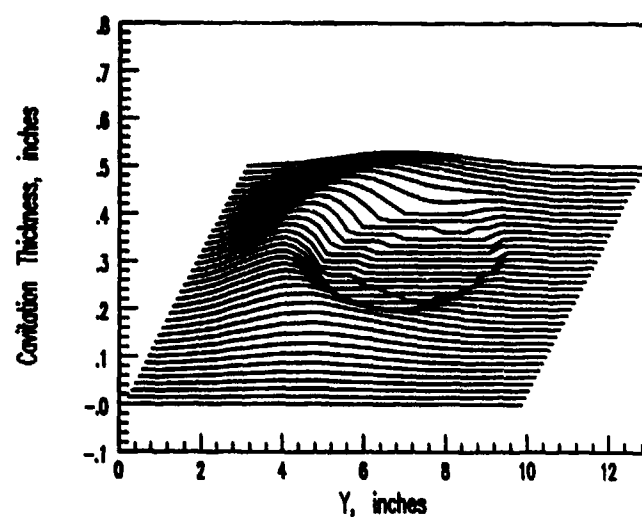
(a) Time = 0.0969 millisecond



(b) Time = 0.192 millisecond



(c) Time = 0.478 millisecond



(d) Time = 0.858 millisecond

FIGURE 41. Spatial Distribution of the Wall Cavitation.

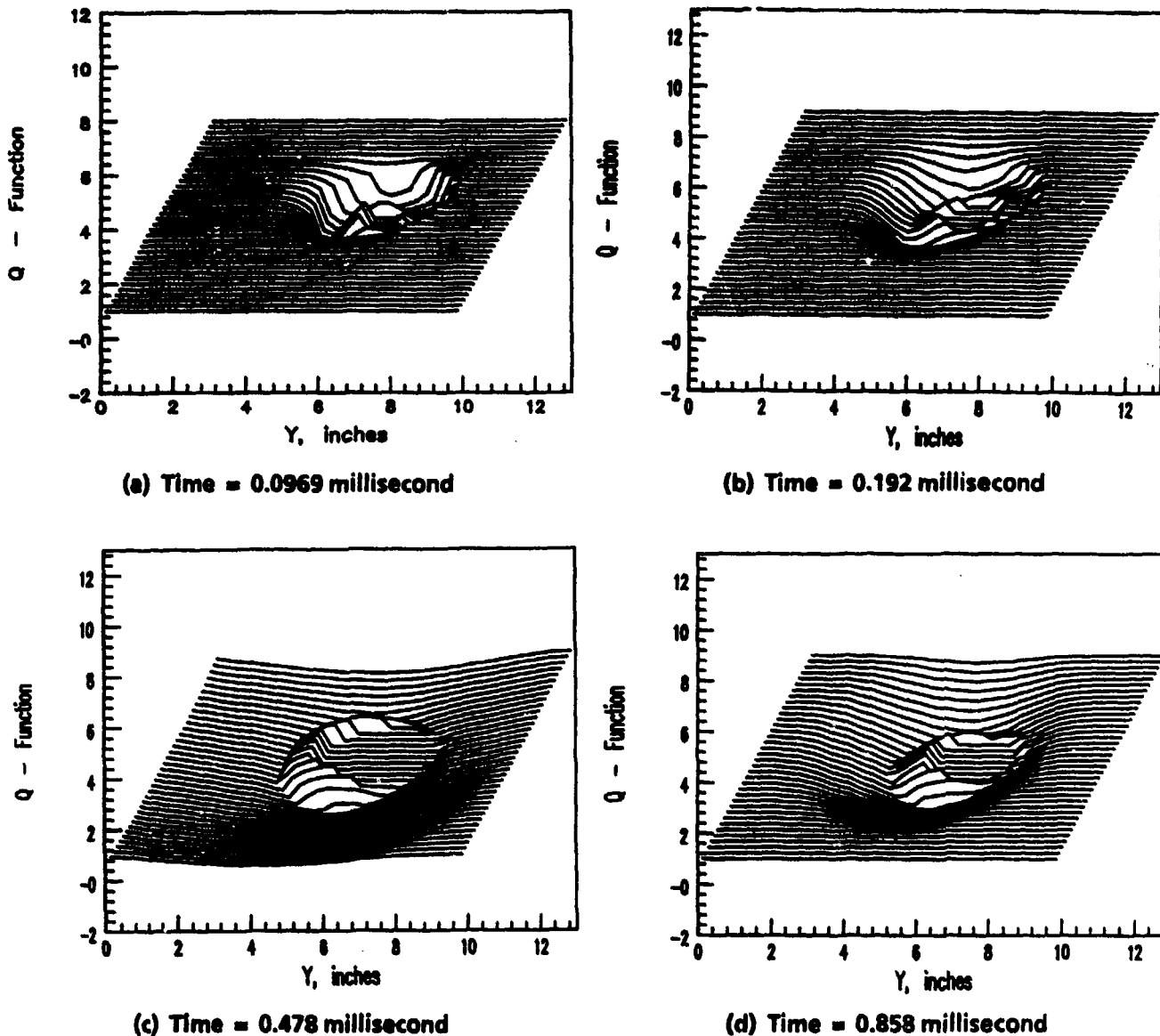


FIGURE 42. Spatial Distribution of the Variable Image Q Function.

WALL FAILURE PREDICTION

The 7075-T6 aluminum alloy used in the experiments is a very brittle material susceptible to crack propagation. In the hydraulic ram testing, little or no damage enhancement is obtained at low projectile impact velocities. As the velocity is increased, a threshold is passed, and the damage increases catastrophically by means of fractures that propagate from the perforation to the edge of the panel. As the projectile velocity is increased further, the number of propagating cracks increases.

NWC TP 6770

A slight modification of classical linear elastic fracture mechanics has been successfully used to predict the residual structural capability of ballistically damaged panel elements. This work is summarized in Reference 17. Panels are ballistically damaged and then stressed to failure on a tensile or compression testing machine. The damage is characterized by the maximum extent of the damage perpendicular to the applied stress. This distance is termed the maximum transverse lateral damage (TLD). The critical stress for crack propagation, σ_c , is given by the expression

$$\sigma_c = \Lambda_c (nTLD/2)^{-1/2} \quad (87)$$

The parameter Λ_c is an effective critical stress intensity factor. For initial damage in the form of a sharp crack, Λ_c is the classical stress intensity factor K_c . In general, Λ_c is slightly larger than K_c and depends on the panel thickness. Reference 17 gives details and data for specific material and penetrator combinations.

It is proposed to use Equation 87 to correlate wall panel failures for hydraulic ram where σ_p is identified with the peak membrane stress. For example, for shot 239 the peak membrane stress is about 45 kpsi (see Figure 28). The TLD is the geometric size of the right cylindrical projectile, taking into account the effect of impact obliquity on the hole size.

To evaluate Equation 87 for hydraulic ram damage prediction, the peak stress was calculated as a function of impact velocity for the four engagement geometries, entrance and exit shots at 0- and 45-degree obliquity (see Table 1). The calculation was performed for both Gaussian and fixed-boundary cosine panel deflection profiles. The results are shown in Figures 43 through 46. In each figure, a line is drawn at the stress level predicted by Equation 87 for panel failure. On each curve in the figures, an open symbol represents a shot at that velocity where the test panel survived. Closed symbols represent catastrophic damage propagation. If Equation 87 holds, then all of the open symbols would lie below the line of predicted panel failure and all of the closed symbols would lie above it.

For entrance shots (Figures 43 and 44), it is not clear whether the cosine or Gaussian deflection profiles are more appropriate. One would expect the Gaussian curve to be best for small panels. From the analysis of shot 239, however, it appears that the 10-inch panel is borderline for this choice. For 0-degree obliquity, the cosine predicted stress curve seems too high, although another data point or two would clarify this. The Gaussian predicted stress is too low; this is reasonable since the clamped plate boundary condition would raise the stress levels in the panel. At 45-degree obliquity, no distinction between the cosine and Gaussian curves can be made because of the sparsity of data near the panel failure point. It should be noted that the entrance wound for the 980-ft/s shot had a crack that extended 0.6 inch away from the edge of the projectile geometric perforation. This would tend to lower the predicted failure stress. In general, the TLD is larger than the geometric perforation, particularly near the ballistic limit of the wall. See Reference 17 for details.

Similar curves and data points for exit panels are shown in Figures 45 and 46, respectively, for 0- and 45-degree obliquity. In both cases the Gaussian curves are too low, and apparently underestimate the stress level at the exit hole. The cosine curves are better, particularly for 45-degree obliquity.

NWC TP 6770

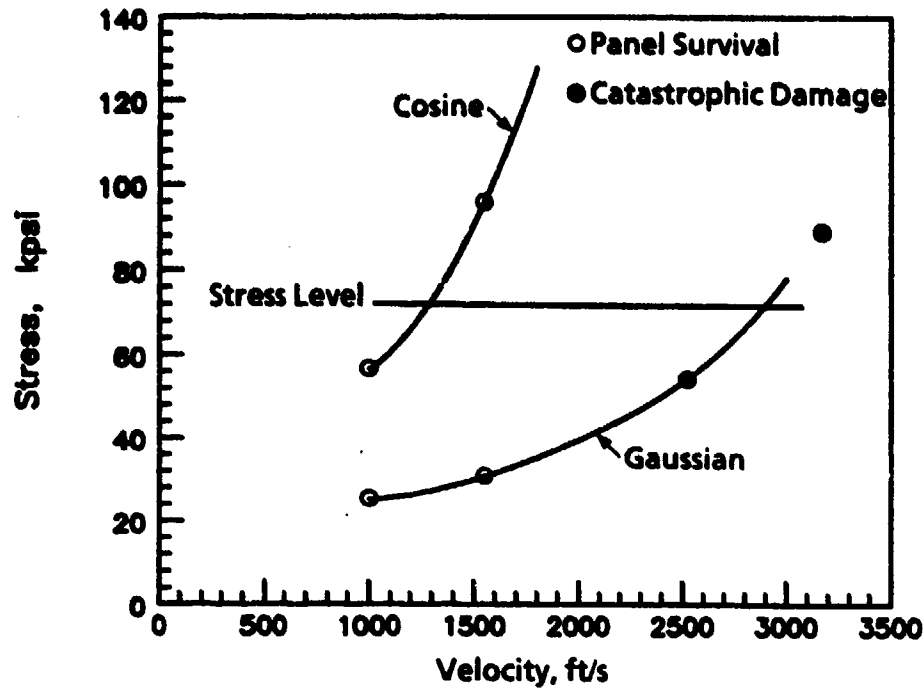


FIGURE 43. Results of Peak Stress Calculation Performed for Both Gaussian and Fixed-Boundary Cosine Panel Deflection Profile Entrance Shot, 0-Degree Obliquity.

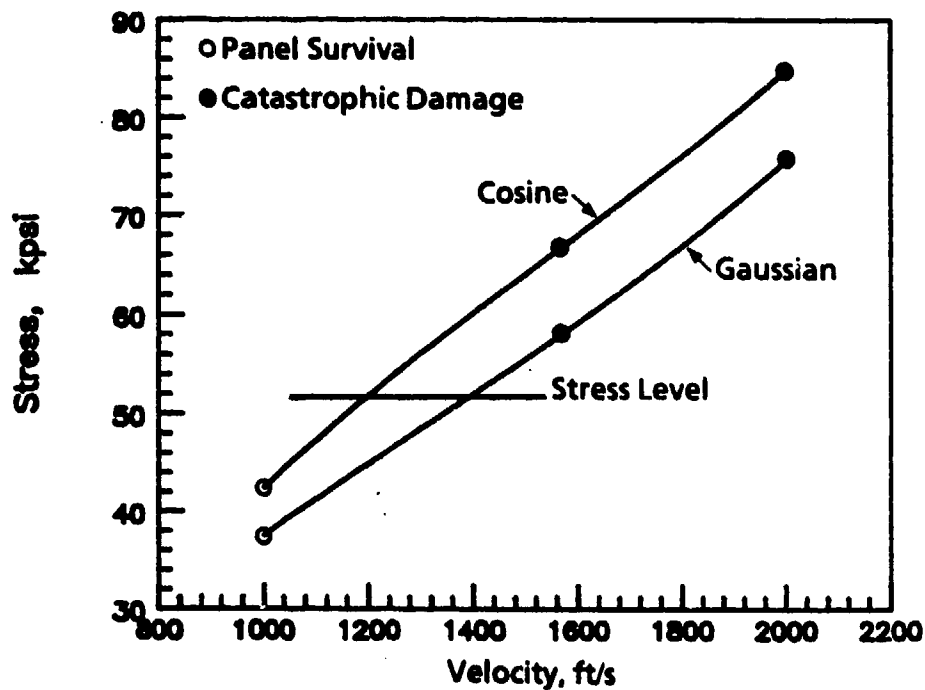


FIGURE 44. Results of Peak Stress Calculation Performed for Both Gaussian and Fixed-Boundary Cosine Panel Deflection Profile Entrance Shot, 45-Degree Obliquity.

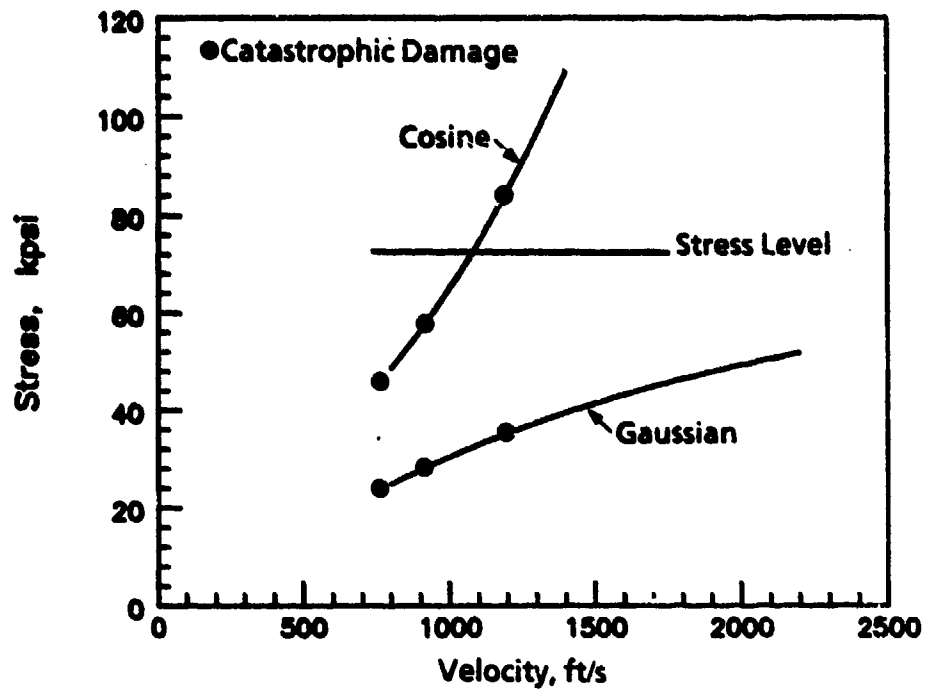


FIGURE 45. Results of Peak Stress Calculation Performed for Both Gaussian and Fixed-Boundary Cosine Panel Deflection Profile Exit Panel, 0-Degree Obliquity.

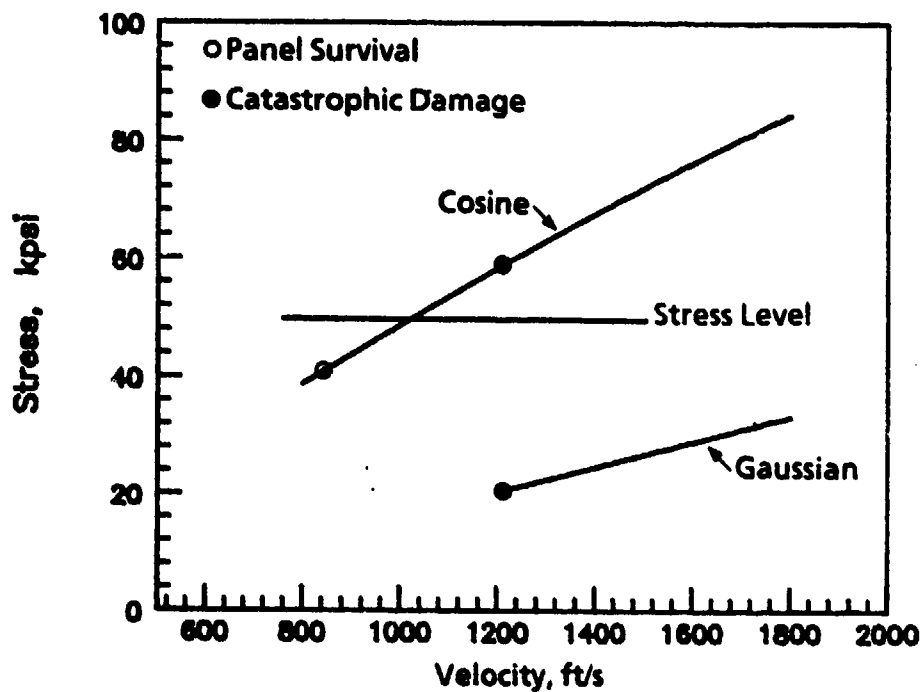


FIGURE 46. Results of Peak Stress Calculation Performed for Both Gaussian and Fixed-Boundary Cosine Panel Deflection Profile Exit Panel, 45-Degree Obliquity.

NWC TP 6770

At 0-degree obliquity, both curves give a much higher stress level than expected, based on fracture mechanics. As a possible explanation of this, the two exit wounds at lower velocities (766 and 893 ft/s) have a different appearance than for the remaining shots in the test series. In all the other tests, a clean puncture was obtained in the shape of the projectile with some possible limited spalling or cracking around the edges--a plugging penetration. For the two low-velocity shots, the panel was only sheared around half of the circumference of the projectile, and then the hole was apparently enlarged by tearing one or more large flaps of material. The exit velocity of the projectile may be approaching the ballistic limit for the panel where the interaction between the wall and penetrator is significant. This interaction is not accounted for in this analysis.

At 45-degree obliquity, the cosine curve gives a good estimate of the failure threshold. The low-velocity shot exit wound was enlarged by limited cracking and spallation. This would tend to lower the predicted failure threshold.

SUMMARY AND CONCLUSIONS

The pressure wave generation model developed in Reference 13 has been extended to multiple supersonic projectiles. The extension to multiple projectiles is based on linear superposition of fluid potentials. The predictions for multiple projectiles are expected to be as good as those for single projectiles; however, no other tests have been performed to verify this.

The predictions for supersonic projectiles are invalid in the forward hemisphere of the projectile because of a mathematical singularity obtained there. Predictions in the rear hemisphere may be of use for entrance wall pressure loading. Preliminary results of analysis of tests with multiple supersonic fragments (not reported here) support this idea.

The variable image model of the fluid/structure interaction has been generalized to the case of pressure-dependent boundary conditions at the fluid/structure interface. This boundary condition applies in several important situations, including cavitation at the wall. Fuel tank hardening concepts, including air gaps and foam isolation layers, can be analyzed with pressure-dependent boundary conditions.

The structural reaction model of References 12 and 15 has been generalized using Lagrange formalism to include more accurate wall deflection shapes and boundary conditions. A variable-width Gaussian shape was found to give acceptable comparison of theory with strain gage records of entrance wall testing.

Nine instrumented hydraulic ram tests were performed to provide pressure and strain data for comparison with analysis. A detailed analysis of an entrance panel shot at 45-degree obliquity was presented comparing theory and experiment. Plots of the pressure-wave propagation within the fluid were presented. Additional plots of the fluid and structural properties at the interface showed details of the hydraulic ram phenomena. The importance of the fluid cavitation at the interface is emphasized.

Predictions are made of the threshold for catastrophic failure of fuel cell walls using the extension of fracture mechanics of Reference 17. The predictions were moderately successful when compared with experimental data. More detailed structural analysis methods should improve the accuracy of the predictions.

NWC TP 6770

REFERENCES

1. Boeing Co. *Hydraulic Ram*, by R. J. Bristow and J. F. Lundeberg. Seattle, Wash., Boeing, February 1969. (FAD S-66, publication UNCLASSIFIED.)
2. McDonnell Douglas Corp. *Hydraulic Ram: A Fuel Tank Vulnerability Study*, by R. Yurkovich. St. Louis, Mo., MDC, September 1969. (Report No. 6964, publication UNCLASSIFIED.)
3. Naval Weapons Center. *Fluid Dynamic Analysis of Hydraulic Ram*, by E. A. Lundstrom. China Lake, Calif., NWC, July 1971. (NWC TP 5227, publication UNCLASSIFIED.)
4. NATO Advisory Group for Aerospace Research and Development. *Fluid Dynamic Analysis of Hydraulic Ram*, by E. A. Lundstrom and W. K. Fung. Neuilly-sur-Seine, France, AGARD, January 1976. (AGARD-CP-186, publication UNCLASSIFIED.)
5. Joint Technical Coordinating Group for Aircraft Survivability. *Fluid Dynamic Analysis of Hydraulic Ram III (Results of Analysis)*, by E. A. Lundstrom and W. K. Fung. Washington, D.C., JTCG/AS, September 1976. (JTCG/AS 74-T-015, publication UNCLASSIFIED.)
6. National Aeronautics and Space Administration. *A Computer Program for the Geometrically Nonlinear Static and Dynamic Analysis of Arbitrarily Loaded Shells of Revolution, Theory and User's Manual*, by R. E. Ball. NASA, April 1972. (NASA CR-1987, publication UNCLASSIFIED.)
7. Air Force Flight Dynamics Laboratory. *Effects of Internal Blast on Combat Airfield Structure. Volume I. Engineer's Manual; Volume II. User's and Programmers's Manual*, by J. Brass, J. R. Yamane, M. J. Jacobson. Wright-Patterson Air Force Base, Ohio, AFFDL, January 1974. (AFFDL-TR-73-136, publication UNCLASSIFIED.)
8. Naval Postgraduate School. *Structural Response of Fluid-Containing Tanks to Penetrating Projectiles (Hydraulic Ram)—A Comparison of Experimental and Analytical Results*, by R. E. Ball. Monterey, Calif., NPS, May 1976. (NPS-57 Bp 7605, publication UNCLASSIFIED.)
9. P. F. Fry, R. K. Newman, and S. J. Bless. "Measurements of Hydrodynamic Ram-Driven Panel Displacements and Comparison With Numerical Predictions by BR1A(HR) and Afton Codes," in *Proceedings of the Hydrodynamic Ram Seminar, May 1977*. P. 503. (AFFDL-TR-77-32, JTCG/AS-77-D-002, publication UNCLASSIFIED.)
10. S. J. Bless, P. F. Fry, and J. P. Barber. "Hydrodynamic Ram Driven Pressure Fields and Panel Displacements for High Velocity Spherical Fragments," in *Proceedings of the Hydrodynamic Ram Seminar, May 1977*. P. 37. (AFFDL-TR-77-32, JTCG/AS-77-D-002, publication UNCLASSIFIED.)
11. E. A. Lundstrom. "Fluid/Structure Interaction in Hydraulic Ram," in *Proceedings of the Hydrodynamic Ram Seminar, May 1977*. P. 223-30. (AFFDL-TR-77-32, JTCG/AS-77-D-002, publication UNCLASSIFIED.)

NWC TP 6770

12. D. P. Ankeney. "Hydraulic Ram Structural Response," in *Proceedings of the Hydrodynamic Ram Seminar, May 1977*. P. 207-21. (AFFDL-TR-77-32, JTCG/AS-77-D-002, publication UNCLASSIFIED.)
13. Joint Technical Coordinating Group for Aircraft Survivability. *Fluid Dynamic Analysis of Hydraulic Ram IV (User's Manual for Pressure Wave Generation Model)*, by E. A. Lundstrom and W. K. Fung. Washington, D. C., JTCG/AS, October 1976. (JTCG/AS 74-T-0180, publication UNCLASSIFIED.)
14. Joint Technical Coordinating Group for Aircraft Survivability. *Hydraulic Ram Structural Response Modification*, by D. P. Ankeney. Addendum to Hydraulic Ram IV. Washington, D. C., JTCG/AS, May 1977. (JTCG/AS 74-T-0180, publication UNCLASSIFIED.)
15. Northrop Corp. *Survivable Design Criteria for Composite Fuel Tanks*, by J. Wada, R. M. Heitz, and M. J. Jacobson. August 1981. Prepared under Contract N00123-78-C-0219 for Naval Weapons Center, China Lake, Calif. (Publication UNCLASSIFIED.)
16. Boeing Co. *Hydraulic Ram Structural Response Computer Program (HRSR)*, by W. M. Herlin and J. G. Avery. September 1981. Prepared under Contract N60530-80-C-0242 for Naval Weapons Center, China Lake, Calif. (Publication UNCLASSIFIED.)
17. Air Force Wright Aeronautical Laboratory. *Design Guide for Survivable Structures in Combat Aircraft*, by S. J. Bradley and J. G. Avery. Wright-Patterson Air Force Base, Ohio, AFWAL, April 1984. (AFWAL-TR-84-3015, publication UNCLASSIFIED.)
18. Air Force Wright Aeronautical Laboratory. *Survivable Composite Integral Fuel Tanks, Volume 1. Manufacturing, Testing, and Analysis*, by M. J. Jacobson, R. M. Heitz, and J. R. Yamane. Wright-Patterson Air Force Base, Ohio, AFWAL, January 1986. (AFWAL-TR-85-3085, publication UNCLASSIFIED.)
19. R. E. Ball and S. L. Fahrenkrog. "Crack Damage in Fluid Containing Tanks Due to Ballistic Penetrators," in *Proceedings of the Hydrodynamic Ram Seminar, May 1977*. P. 475. (AFFDL-TR-77-32, JTCG/AS-77-D-002, publication UNCLASSIFIED.)
20. University of Dayton Research Institute. *A Model for Hydrodynamic Ram Failure Based on Fracture Mechanics Analysis*, by Z. Rosenberg and S. Bless. Dayton, Ohio, UDRI, April 1985. (UDRI-TR-8530, publication UNCLASSIFIED.)

- 2 Naval Air Programs Council
AIP-PLAN, D. B. Johnson (1)
AIP-STAFF, D. B. Johnson (1)
- 2 Naval Air Development Center, Washington (Code 603, T. E. Nease)
- 1 Naval Postgraduate School, Monterey (Code AFDP, Prof. R. E. Hall)
- 2 Air Ballistic Research Lab, Dayton, Ohio, USAF Langley Research Center (NACOR-PL-A,
Dr. R. H. Bishop)
- 1 Langley Research Center, Langley Field, VA, USAF Langley Research Center (Dr. J. Perkins)
- 1 Army Corps of Engineers, Fort Belvoir, MO, USAF Langley Research Center (Dr. T. Seibler)
- 2 Air Force Research Division, Wright-Patterson Air Force Base (AFAPL/SAB, G. C. Crane)
- 2 Air Force Wright Aeronautical Laboratories, Wright-Patterson Air Force Base
AFAPL/WRLAB, F. D. Zettling (1)
AFAPL/WRLAB, G. J. Gonsky (1)
- 1 Defense Intelligence Information Center, Alexandria
- 1 Bell Telephone - Western, Port North, TX (D. Larson)
- 1 Spun, Allen and Hamilton Incorporated, Wright-Patterson Air Force Base (D. L. Orphal)
- 1 Chase Corporation, Alexandria, VA (D. A. Riegels)
- 1 Defense Research Institute, University of Denver, Denver, CO (R. F. Nacht)
- 1 General Aircraft Systems Division, Rochester, NY (Dr. H. Garnet)
- 2 McDonnell Aircraft Company, St. Louis, MO
B. O. Hanberry (1)
M. P. Jones (1)
D. Wilson (1)
- 3 Westinghouse Corporation, Elkhart, IN
E. L. Christensen (1)
H. Jacobson (1)
L. McLeod (1)
- 2 Westinghouse Corporation, Palo Alto, CA
W. D. Rutledge (1)
J. C. Swanson (1)
S. C. Wallin (1)
- 1 Southwest Research Institute, San Antonio, TX (P. H. Zahel)
- 1 The Boeing Company, Philadelphia, PA (J. L. Grubb)
- 1 The Boeing Company, Seattle, WA (R. J. Brinson)
- 1 The Boeing Company, Wichita, KS (J. G. Avery)
- 1 University of Dayton, Dayton, OH (S. J. Blom)